Interactions of Hydraulic Fractures With Grain Boundary Discontinuities in the Near Wellbore Region

Keita Yoshioka[1,2] , **Masafumi Katou[3]** , **Kohei Tamura[3], Yutaro Arima[3], Yoshiharu Ito[3], Youqing Chen[4]** , **and Tsuyoshi Ishida[4]**

[1]Helmholtz Centre for Environmental Research—UFZ, Leipzig, Germany, [2]Montanuniversität Leoben, Leoben, Austria, [3]Japan Organization for Metals and Energy Security, Tokyo, Japan, [4]Kyoto University, Kyoto, Japan

Abstract Hydraulic fractures often turn or branch, interacting with preexisting discontinuities in the rock mass (e.g., natural fractures or defects). The criteria for fracture penetration or deflection are typically based on the in situ stress, and the angle and strength of discontinuities. However, in hydraulic fracture experiments on carbonate rocks (Naoi et al., 2020, https://doi.org/10.1093/gji/ggaa183), small scale analyses show that the fractures deflected more frequently at discontinuities (grain boundaries) as they propagated farther from the wellbore, a finding not explained by the conventional criteria. Here, we demonstrate that the energy dissipation of a deflecting fracture increases with the distance from the wellbore, such that a propagating hydraulic fracture more easily deflects at a discontinuity from an energetic standpoint. This tendency was confirmed by hydraulic fracture simulations based on a successive energy minimization approach. Our findings, which show that wellbores appreciably affect the behavior of hydraulic fractures, highlight the importance of energetic stability analysis for determining fracture paths.

Plain Language Summary Hydraulic fractures may form complex patterns as they grow outward from a wellbore by turning or deflecting when they interact with preexisting discontinuities in rocks. Because complex fractures enhance the permeability of rock formations more effectively than planar fractures, many studies have investigated how a fracture interacts with a preexisting discontinuity such as a natural fracture. The fate of a growing fracture at a discontinuity—whether it penetrates or deflects—is typically judged based on the in situ subsurface stress, and the characteristics of the discontinuity. However, we observed in experiments that fractures deflected more often at discontinuities (grain boundaries) as they propagated farther away from the wellbore, which cannot be explained by the conventional criteria. To explain these observations, we analyzed the energy expenditure of a deflecting fracture and showed that it becomes energetically more favorable for a fracture to deflect at a discontinuity as it grows farther away from the wellbore. We confirmed this insight by using numerical simulations. We thus caution that the conventional criteria may not be applicable in the near wellbore region, and we suggest that energetic stability, rather than the local stress at the fracture tip, should be analyzed to determine fracture paths.

1. Introduction

The propagation direction of hydraulically induced fracture was contested at some point (Harrison et al., 1954; Reynolds et al., 1961) whether it is horizontal along a bedding plane lifting the overburden (Howard & Fast, 1950) or orthogonal to the minimum principal stress (Hubbert & Willis, 1957). However, a number of theoretical analyses and experiments demonstrated that the plane of hydraulic fracture propagation is orthogonal to the minimum principal stress (Harrison et al., 1954; Hubbert & Willis, 1957). Based on this notion, hydraulic fracturing has become an established means to estimate the minimum principal stress as the fracture planes open against the minimum principal stress (Abou-Sayed et al., 1978; Baumgärtner & Zoback, 1989; Haimson & Fairhurst, 1969) or even the intermediate principal stress (Schmitt & Zoback, 1989), though debates on pressure interpretation are yet to be settled (Bröker & Ma, 2022; F. Guo et al., 1993; Jung et al., 2016; Kamali & Ghassemi, 2019). A thorough review on this subject is provided by Schmitt and Haimson (2017).

However, when hydraulic fractures interact with preexisting discontinuities (e.g., natural fractures or defects in the rock mass), the propagation of fractures may deviate from the direction orthogonal to the minimum principal stress. Microseismic records from hydraulic fracturing of tight hydrocarbon formation show that clouds of seismic events extended beyond the plane orthogonal to the principal minimum stress direction (Fischer

Supervision: Tsuyoshi Ishida
Validation: Keita Yoshioka
Visualization: Keita Yoshioka, Masafumi Katou, Youqing Chen
Writing – original draft: Keita Yoshioka
Writing – review & editing: Keita Yoshioka, Masafumi Katou, Kohei Tamura, Yutaro Arima, Yoshiharu Ito, Youqing Chen, Tsuyoshi Ishida

et al., 2008; Warpinski & Teufel, 1987). Similar observations were also made in geothermal well stimulation (Cladouhos et al., 2016; Cuenot et al., 2008; Kraft & Deichmann, 2014). Furthermore, mine–back experiments (Jeffrey & Weber, 1994; Jeffrey et al., 2009) and retrieved cores from the in situ hydraulic fracturing test (Ciezobka et al., 2018) confirmed such fracture deviation and interaction with discontinuities. Understanding of such complex fracture behaviors is crucial for well stimulation whose main goal is to increase formation permeability in the near wellbore (Riffault et al., 2018). And to achieve that, induced hydraulic fractures are to interact with preexisting discontinuities to increase their morphological complexities (Cipolla et al., 2008; S. Li et al., 2019).

To study the influence of the preexisting fracture geometry and the applied confining pressure on the direction of hydraulic fracture propagation, Lamont and Jessen (1963) conducted hydraulic fracture experiments with a preexisting fracture. They concluded that the fracture propagation direction is mostly orthogonal to the minimum principal stress and deviates only slightly impacted by the preexisting fracture. Their findings are not aligned with many of the studies reported later. One possible explanation could be that the injection rate, which was not reported in Lamont and Jessen (1963), may have been too high for stable fracture propagation (Q. Zhang et al., 2021). Their study was followed by many experimental works that focused on impacts of the approaching angle, differential stress and strength of the preexisting fracture on the hydraulic fracture propagation (Additionally, injection rate and fluid viscosity impact hydraulic fracture interaction with a preexisting fracture for viscous dominated fracture propagation (Chuprakov et al., 2014; Llanos et al., 2017). In this study, however, our focus is on toughness dominated fracture propagation. For fluid effects, see Section 5.) (Blanton, 1982; Dehghan et al., 2015; T. Guo et al., 2014; Lee et al., 2015; Meng et al., 2010; Warpinski & Teufel, 1987; Yushi et al., 2016; Zhao et al., 2022; Zhou et al., 2008). Q. Zhang et al. (2021) provides a comprehensive review on experimental studies. Furthermore, hydraulic fracture interaction has been studied by numerically (Dahi-Taleghani & Olson, 2011; Fatahi et al., 2017; Lepillier et al., 2020; McClure & Horne, 2014; K. Wu & Olson, 2016). We refer to Dahi-Taleghani et al. (2016) and Lecampion et al. (2018) for reviews on numerical aspects on this subject.

Most existing studies have reported that interactions of hydraulic fractures with discontinuities are largely controlled by the in situ stress, and the geometry and strengths of the discontinuity. Using these parameters, studies have formulated criteria for fracture penetration/deflection in terms of the stress (Blanton, 1982; Chuprakov et al., 2014; Fu et al., 2018; Gu et al., 2012; S. Li et al., 2017; Renshaw & Pollard, 1995; Warpinski & Teufel, 1987) or the energy (Dahi-Taleghani & Olson, 2014; X. Li et al., 2020; Zeng & Wei, 2017). These studies have established that a fracture is more likely to deflect at a discontinuity if either of these decreases: (a) the approaching angle to the interface, (b) the interface strength, or (c) the differential stress.

However, these criteria may not apply straightforwardly to the behaviors of hydraulic fractures in the near wellbore region. Grain scale images from hydraulic fracturing experiments on carbonates (Naoi et al., 2020) have shown that hydraulic fractures deflect more frequently at discontinuities (grain boundaries) as they propagate farther from the wellbore (Figure 1). We can postulate that weakly bonded grain boundaries act as defects and cause the fractures to deflect, as reported in other experimental studies on granites (Chen et al., 2015), but we cannot deduce that grain boundaries are coincidentally weaker farther from the wellbore.

Though Naoi et al. (2020) remarked the increasing fracture complexity away from the wellbore, their study focused on the failure mechanisms from moment tensor analyses and no quantitative analyses of fracture morphology or computation on fracture propagation was performed. In this study, our objective is to investigate their experimental observations from an energetic perspective. Our contributions are three-hold. First, we analyzed the fracture paths quantitatively using digitized images from the experiments in Naoi et al. (2020) including unpublished results. Second, we computed energy release rates of deflecting and penetrating fractures with varying distances from the wellbore using the potential energy differences induced by fracture tip perturbations. Third, we numerically simulated hydraulic fracture interactions with a discontinuity (grain boundary) using an approach based on successive energy minimization (Bourdin et al., 2012). The results of the energy release rate analysis and the numerical simulations hydraulic fracture propagation agree well with the experimental observations, indicating that the fracture propagation path is affected not only by the in situ stress, and the geometry and strength of discontinuities (grain boundaries), but also by the distance from the wellbore.
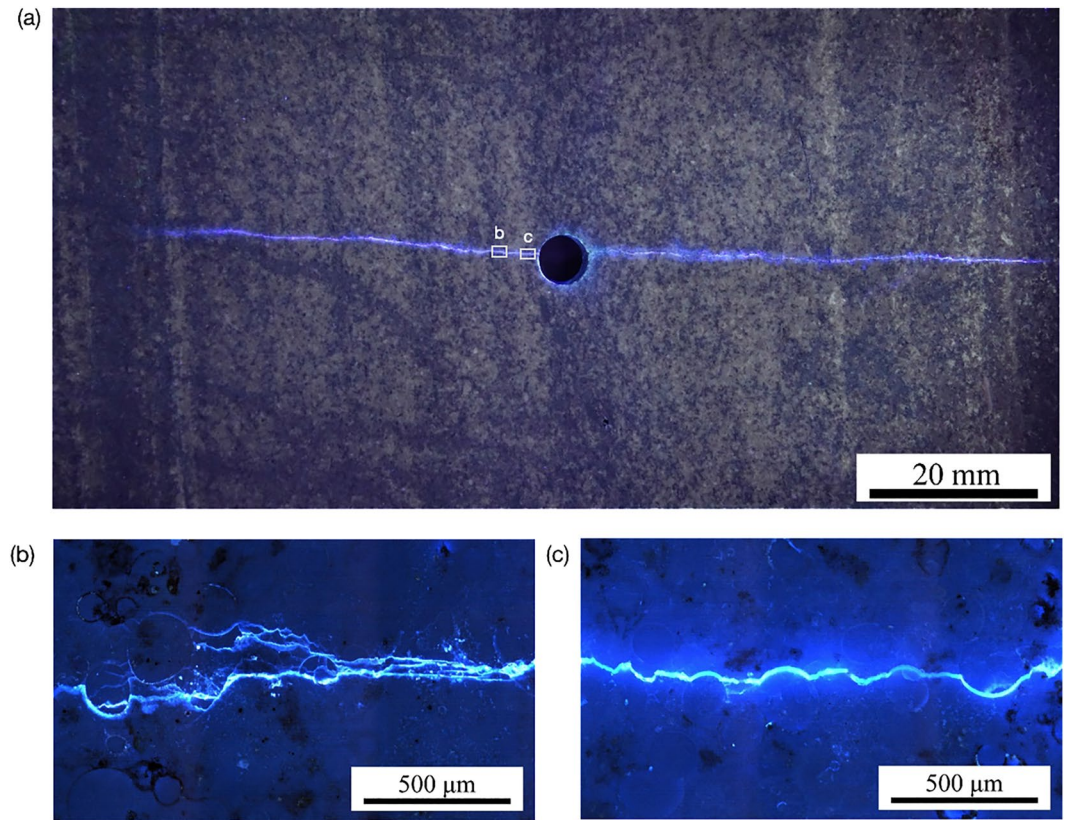
Figure 1. Hydraulic fractures deviation from the straight path and increasing their topological complexity with the distance away from the wellbore (modified from Chen et al. (2018) and Naoi et al. (2020)). (a) A cut section under natural and ultraviolet light. The location of the zoomed in images in (b) and (c) are indicated with white boxes in (a). See Section 2.2 for our quantification of fracture complexity.

2. Fracture Path Analysis

We analyzed fracture paths observed in three samples from the hydraulic experiments conducted in Naoi et al. (2020). For experimental and property measurement details, we refer to Supporting Information S1 and only brief experimental procedures are provided here.

2.1. Experimental Procedures

Hydraulic fracture experiments were conducted on outcrop samples of Eagle Ford formation, a carbonate rock from Langtry, Texas, USA. The samples have a representative Young's modulus (E) of 50 GPa and a Poisson's ratio (ν) of 0.33 measured perpendicular to the direction of sedimentary plane. The porosity is estimated to be lower than 1%. X-ray diffraction analysis indicates that they consist of 96.3% calcite and 3.7% quartz. Although their mineral composition is nearly homogeneous, the samples include textural heterogeneity in the form of calcite microfossils, as seen in thin sections (Figure 2a). These inclusions are expected to have similar mechanical properties to the bulk rock, except that the grain boundaries may not be bonded perfectly.

The total of three samples were prepared with dimensions of 65 mm × 65 mm × 130 mm ([−32.5 mm, +32.5 mm] × [−32.5 mm, +32.5 mm] × [−65 mm, +65 mm]) with a wellbore 3 mm in radius drilled in the center (Figure 2b). The top and bottom surfaces were subjected to an axial loading of 5 MPa, and the other surfaces were not loaded. The wellbore was sealed with a packer which has a 30 mm pressurizing section ($x = -15$ to $+15$ mm) sealed with two O-rings. Through this open section, a thermosetting acrylic (methyl methacrylate) resin with a viscosity (It is comparable to the water viscosity at 20°C (1.0 mPa·s).) of 0.8 mPa·s was injected to induce fractures. The resin contained a fluorescent compound so that hydraulically induced fractures can be distinguished from preexisting fractures by their brightness in a thin section under ultraviolet light (Chen et al., 2018; Ishida
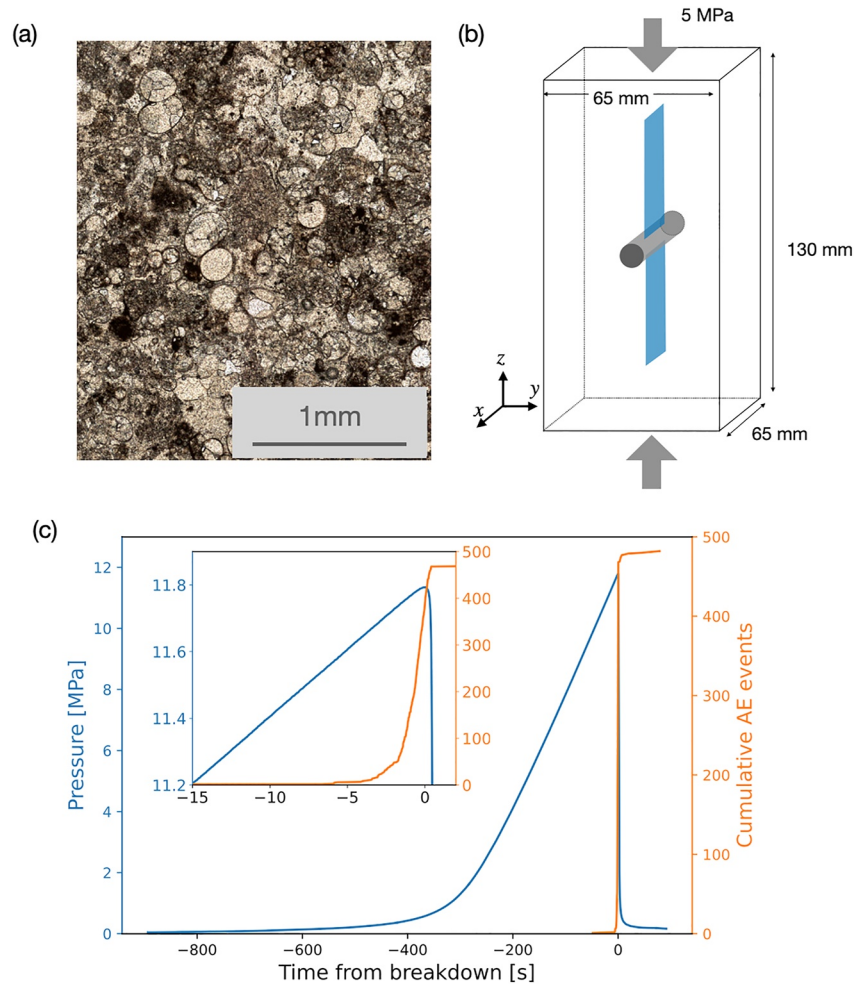
Figure 2. (a) A thin section image of the experimental rock showing oolitic inclusions. (b) Dimensions of the experimental samples. The top and bottom surfaces were subjected to an axial loading of 5 MPa and the other surfaces were not loaded so that fractures propagate on the x–z plane as depicted with the blue planes. (c) Pressure responses and record of acoustic emissions (AEs) from sample #1. The pressures increased almost linearly and failed abruptly. The concentrated AEs at the point of failure indicate the brittle and linear elastic behavior of the sample.

et al., 2016) (Figure 1). And the limit of detection is reported to be less than a few micrometers (Nishiyama & Kusuda, 1994).

Figure 2c shows the response of pressures and acoustic emissions from one of the experiments (sample #1). The hydraulic pressure increased almost linearly and dropped abruptly at the onset of fracturing. This brittle and linear elastic behavior is consistent with the concentration of acoustic emissions around the point of failure. The peak (breakdown) pressures from sample #1, #2, and #3 were 11.79, 10.30, and 10.71 MPa respectively. The fractured samples were heated immediately to harden the resin (Chen et al., 2018). The thin sections were then prepared at the central cross-section (i.e., $x = 0.0$ mm) and we analyzed fractures propagating roughly along the z-axis.

2.2. Fracture Propagation Paths

We examined the thin sections of the experimental specimens under ultraviolet light and studied the fractures connected to the wellbore, classifying long fractures with bright fluorescence as main fractures and short, deflected fractures as branch fractures (Figure 3). When the whole fracture is connected, we picked the brighter fluorescence (wider fracture aperture) as main. Finally, all the identified fractures were visually confirmed as some calcites also have fluorescent properties.
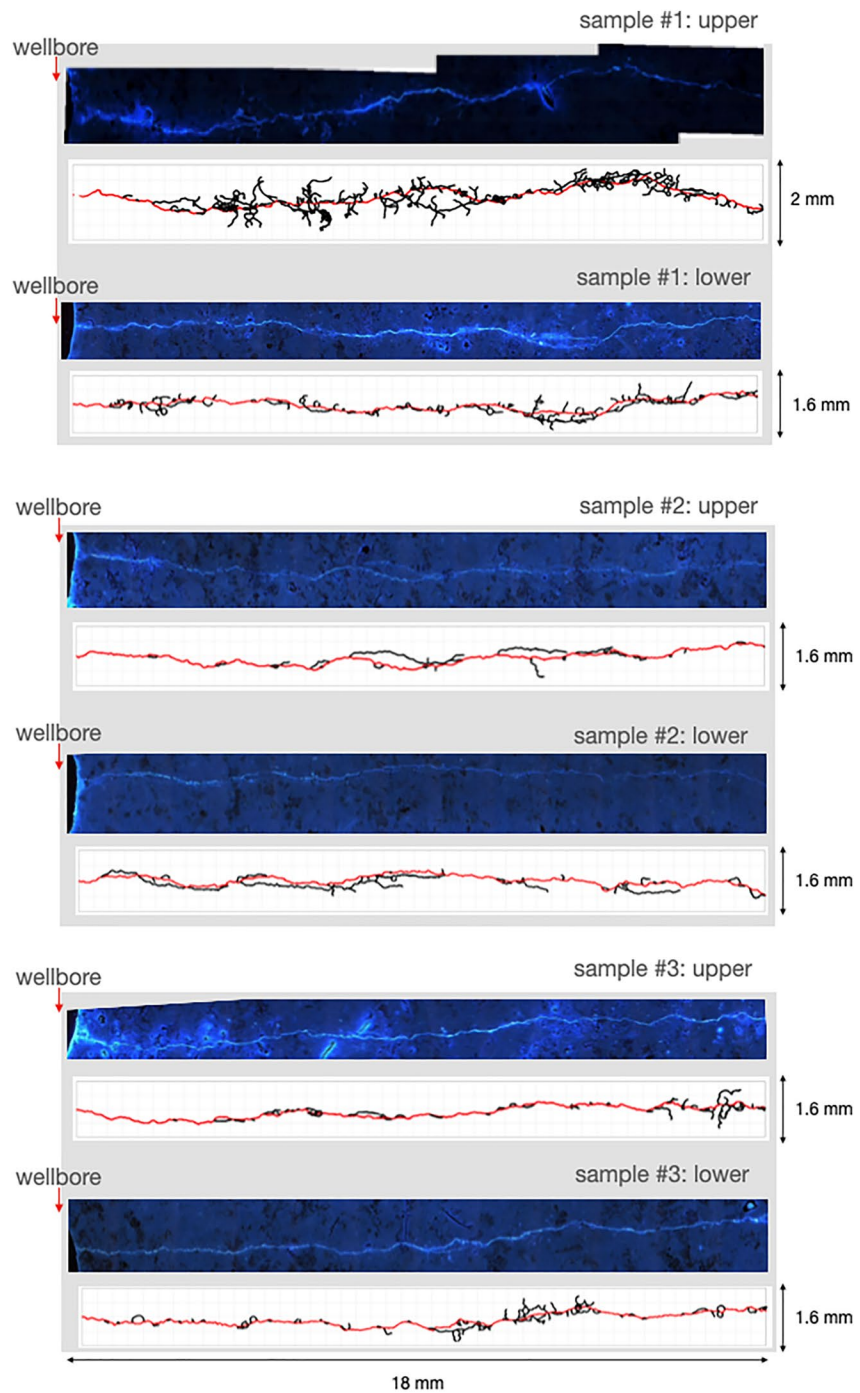
Figure 3. Thin sections of three samples showing resin-filled hydraulic fractures fluorescing blue under ultraviolet light. Red arrows indicate the edge of the wellbore. Beneath each image is a plot showing the main (red) and branch (black) fractures. Sample #1, #2, and #3 were called EFS1701, EFS1704, and EFS1706 respectively by Naoi et al. (2020). "Upper" represent the upper half of a sample and "lower" the lower half of a sample.

In these images, the fractures appear to have increased in topological complexity as they propagated farther from the wellbore. To investigate this apparent change, we calculated the main fracture lengths (L_m) and the total fracture lengths (L_t) against the distance from the wellbore (d). L_t is the sum of the branch and main fracture lengths and thus $L_t \geq L_m$. As shown in Figure 4, we divided the images laterally into 10 µm intervals in the direction of fracture propagation, measured the fracture lengths within each interval, and then determined the total fracture

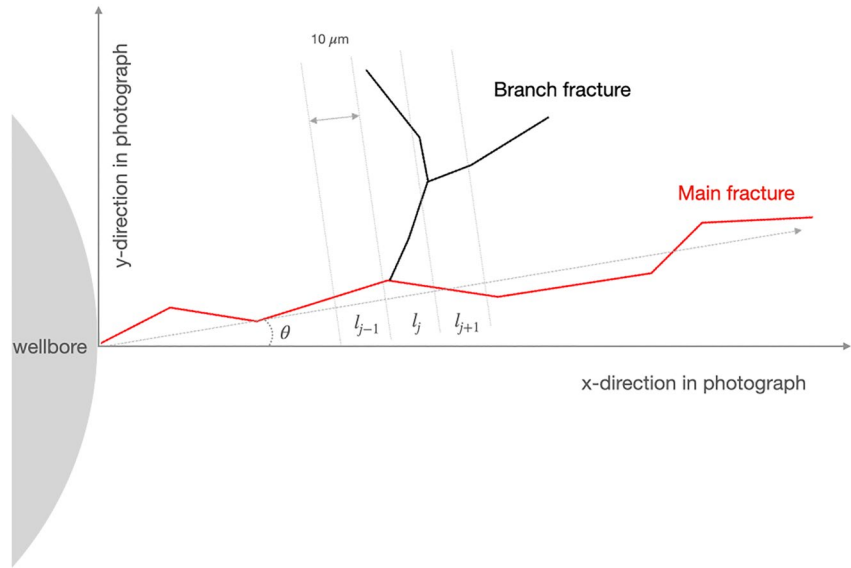**Figure 4.** Quantification of fracture paths. First, the overall propagation direction, θ, is determined and 10 μm intervals are defined; then the measured lengths of the main and branch fractures in the intervals are integrated to yield total fracture lengths. x- and y- directions correspond to Figure 3. The fracture propagation angles θs in Figure 3 are: $-3.3°$ for sample #1 upper, $0.31°$ for sample #1 lower, $7.9°$ for sample #2 upper, $2.3°$ for sample #2 lower, $2.1°$ for sample #3 upper, and $1.7°$ for sample #3 lower.

lengths by summing all of the intervals (see Appendix A for the detailed procedure). For a measure of fracture complexity, we normalized the total fracture length against the corresponding main fracture length as L_t/L_m. This measure has the value 1 ($L_t/L_m = 1$) until the first deflection, after which the fracture complexity increases if branch fractures take longer paths than the main fracture and decreases otherwise.

When the main fracture lengths L_m are plotted against the normalized distance from the wellbore (d/r_o, where r_o is the wellbore radius of 3 mm), the main fractures all fall on a nearly identical linear trend (Figure 5a). When the normalized total fracture lengths L_t/L_m are plotted against d/r_o (Figure 5b), the fracture complexities initially increase with d/r_o to values as high as about 4.5, but they reach a plateau of complexity at a distance between one-half and twice the wellbore radius ($d/r_o = 0.5 - 2$ or $d = 1.5 - 6$ mm).
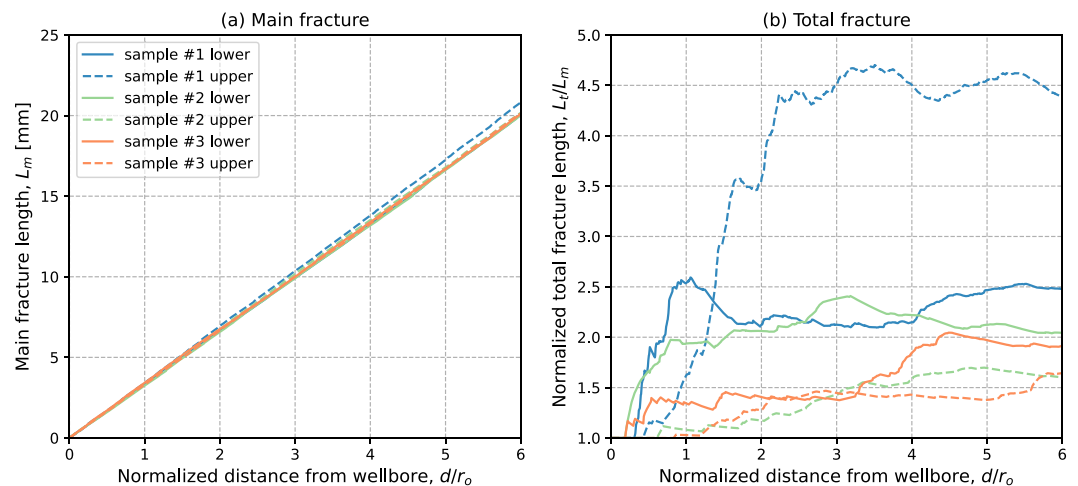

Figure 5. (a) Lengths of main fractures (L_m) against the distance from the wellbore normalized by the wellbore radius (d/r_o). (b) Lengths of total fractures normalized by the corresponding main fracture lengths (L_t/L_m) against the normalized distance d/r_o.

3. Fracture Propagation Mechanism

3.1. Revisiting the Griffith Criterion

The Griffith criterion (Griffith, 1921) states that a line fracture of length l propagates when the energy release rate reaches a critical value,

$$\mathcal{G} = G_c, \tag{1}$$

where G_c is the critical energy release rate and $\mathcal{G}$ is the energy release rate, defined as the released potential energy (Π) with respect to fracture growth:

$$\mathcal{G} := -\frac{\partial \Pi}{\partial l}. \tag{2}$$

While G_c is a measure of material resistance against fracturing (material property), $\mathcal{G}$ is dependent on the fracture geometry and applied loadings. The Griffith criterion is complete with the irreversibility of fracture, meaning that the fracture length only increases. With more recent mathematical tools, we can view Griffith's arguments as a constraint minimization problem known as the Karush-Kuhn-Tucker conditions (Nocedal & Wright, 2006). By denoting the rate of length growth as $\dot{l} \geq 0$, we can rewrite the Griffith criterion as,

$$\dot{l} \geq 0, \quad \mathcal{G} \leq G_c, \text{ and } (\mathcal{G} - G_c)\dot{l} = 0. \tag{3}$$

Francfort and Marigo (1998) recast the Griffith criterion Equation 1 as a minimization problem where the displacement $\mathbf{u}$ and the crack set Γ are to be determined from

$$(\mathbf{u}, \Gamma) = \arg\min_{\mathbf{u},\Gamma} \mathcal{E}(\mathbf{u}, \Gamma), \tag{4}$$

where the total energy $\mathcal{E}$ is the sum of the potential energy and the fracture surface energy:

$$\mathcal{E}(\mathbf{u}, \Gamma) := \Pi + \int_\Gamma G_c \, d\Gamma. \tag{5}$$

From Equation 4, we can view the Griffith criterion as a special instance of the case in which the energy is minimized only along the prescribed fracture path l:

$$(\mathbf{u}, l) = \arg\min_{\mathbf{u},l} (\Pi + G_c l). \tag{6}$$

Then we can recover the Griffith criterion from the first-order minimization condition,

$$\frac{\partial (\Pi + G_c l)}{\partial l} = \frac{\partial \Pi}{\partial l} + G_c = 0. \tag{7}$$

3.2. The Griffith Criterion in Terms of Stress

The Griffith criterion Equation 1 is often applied in terms of stress using the concept of stress intensity factor, K, through Irwin's formula (Irwin, 1957). Here we note a few identities between the energy-based (Griffith's) and stress-based (Irwin's) approaches.

For a line crack, $\Gamma = [-l, l] \times \{0\}$, subjected to a tensile (mode-I) loading in an infinite 2D domain, the energy release rate defined in Equation 2 can be equivalently expressed using the stress intensity factor as,

$$\mathcal{G} = \frac{K_I^2}{E'}, \tag{8}$$

where $E' = E/(1 - \nu^2)$ for plane strain and $E' = E$ for plane stress, and K_I is the (mode-I) stress intensity factor, defined in polar coordinates (r, θ) as (Anderson, 1995),

$$K_I := \lim_{r \to 0} \sqrt{2\pi r} \sigma_{yy}(r, 0). \tag{9}$$

Accordingly, Griffith's fracture propagation criterion in Equation 1 can be written using the stress intensity factor as

$$K_I = K_{Ic},\tag{10}$$

where K_{Ic} is the critical stress intensity factor for mode-I fracture. As the energy release rate ($\mathcal{G}$) is expressed in terms of the mode-I stress intensity factor (K_I) in Equation 8, the critical energy release rate (G_c) can be expressed in terms of the mode-I stress intensity factor (K_{Ic}) as

$$G_c = \frac{K_{Ic}^2}{E'}.\tag{11}$$

Both G_c and K_{Ic} represent the material's resistance to fracturing and are related through Equation 11. And, interchangeably, they are often referred to as "fracture toughness."

In the following, we analyze fracture behaviors using the energy release rate rather than the stress intensity factor(s), but the energy release rate can be converted from the stress intensity factors. More generally, when all modes of loadings (I, II, and III) are present, the energy release rate is,

$$\mathcal{G} = \frac{K_I^2 + K_{II}^2}{E'} + \frac{K_{III}^2}{2\mu},\tag{12}$$

where K_{II} and K_{III} are the stress intensity factors for shear (mode-II) and tearing (mode-III) loadings, respectively, and μ is the shear modulus. From Equation 12, we can see that an increase in the energy release rate means an increase in the stress intensity factor and vice versa.

3.3. Fracture Path Determination

In which direction will a fracture propagate under multidirectional loadings? The two main approaches to this question are the principle of local symmetry (Cotterell & Rice, 1980; Gol'dstein & Salganik, 1974) and the maximum energy release rate (Hussain et al., 1974; Nuismer, 1975). Under mode-I (tensile) and mode-II (shear) loadings, for example, the principle of local symmetry mandates model-I propagation, where the mode-II stress intensity factor is zero ($K_{II} = 0$), whereas the maximum energy release rate approach seeks to determine the direction that maximizes the energy release rate.

These two approaches predict a similar propagation direction (identical for smoothly growing cracks and almost identical for kinking cracks) in isotropic, homogeneous materials (Amestoy & Leblond, 1992; Cotterell & Rice, 1980; Hutchinson & Suo, 1991; Nuismer, 1975), but the principle of local symmetry does not correctly predict propagation paths in anisotropic or heterogeneous materials (Brach et al., 2019; Marder, 2004; Takei et al., 2013). In contrast, the maximum energy release rate approach can predict the right direction if we consider the energy dissipation associated with a material heterogeneity (Chambolle et al., 2009; Gurtin & Podio-Guidugli, 1998; Hakim & Karma, 2009; He & Hutchinson, 1989; B. Li & Maurini, 2019; Takei et al., 2013). This modified (or generalized) energy release rate approach seeks a direction that maximizes the energy dissipation as

$$\max_{\alpha \in [0, 2\pi)} \frac{\mathcal{G}(\alpha)}{G_c(\alpha)},\tag{13}$$

where α is the propagation angle we wish to find.

Let us consider a fracture arriving at an inclined interface (e.g., a natural fracture) with an angle of β (Figure 6a), where the interface has a different fracture toughness from the bulk material given by

$$G_c(\alpha) = \begin{cases} G_c^{\text{int}}, & \text{for } \alpha = \beta \\ G_c^{\text{bulk}}, & \text{otherwise} \end{cases}\tag{14}$$

where G_c^{int} and G_c^{bulk} are the fracture toughness of the interface and the bulk material, respectively.

He and Hutchinson (1989) computed the energy release rate $\mathcal{G}(\alpha)$ of a deflecting fracture under mode-I loading and normalized it against the energy release rate $\mathcal{G}(0)$ of a straight fracture propagation. The normalized energy release rate $\mathcal{G}(\alpha)/\mathcal{G}(0)$ depends only on the deflection angle α:
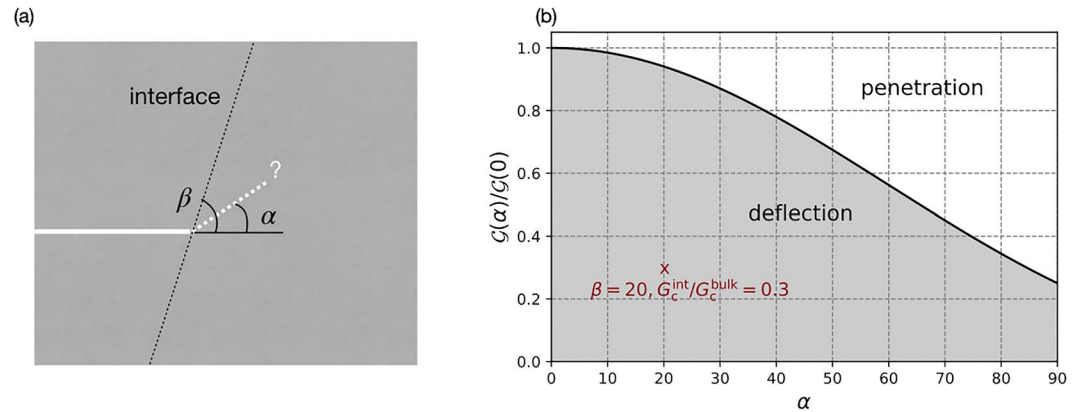
Figure 6. (a) A fracture arriving at an interface at angle β with a possible propagation angle α. (b) Energy release rates of a deflecting fracture normalized by the energy release rate of a penetrating fracture, plotted against the propagation angle α. The shaded region corresponds to fracture deflection and the unshaded region corresponds to fracture penetration; the line between them corresponds to the He and Hutchinson criterion (see the text for details). The point marked by "x" represents an interface angle of 20° and an interface fracture toughness of 30% of the bulk fracture toughness, which lies in the deflection region.

$$\frac{\mathcal{G}(\alpha)}{\mathcal{G}(0)} = \frac{1}{16}\left[\left(3\cos\frac{\alpha}{2} + \cos\frac{3\alpha}{2}\right)^2 + \left(\sin\frac{\alpha}{2} + \sin\frac{3\alpha}{2}\right)^2\right], \tag{15}$$

which is plotted in Figure 6b against α. We can see from Equation 15 that the energy release rate is always the greatest with straight fracture propagation ($\mathcal{G}(0) \geq \mathcal{G}(\alpha)$). Thus, the energy dissipation of straight propagation ($\alpha = 0$) is always greater than those of other propagation angles except for the direction of the interface ($\alpha = \beta$), which leads to:

$$\max_{\alpha \in [0,2\pi),\, \alpha \neq \beta} \frac{\mathcal{G}(\alpha)}{G_c(\alpha)} = \frac{\mathcal{G}(0)}{G_c^{\text{bulk}}}. \tag{16}$$

This result leads us to two possibilities, $\alpha = \beta$ or 0. And whether the energy dissipation along the interface, $\mathcal{G}(\beta)/G_c^{\text{int}}$, is greater than that of straight propagation, $\mathcal{G}(0)/G_c^{\text{bulk}}$, depends on G_c^{int} and G_c^{bulk}. Using this criterion, we can determine whether the fracture deflects or penetrates by simply comparing the respective energy dissipations of deflection and straight propagation (Xu et al., 2003). In other words,

$$\begin{cases} \dfrac{\mathcal{G}(0)}{G_c^{\text{bulk}}} < \dfrac{\mathcal{G}(\beta)}{G_c^{\text{int}}} & \rightarrow \text{deflection} \\[2mm] \dfrac{\mathcal{G}(0)}{G_c^{\text{bulk}}} > \dfrac{\mathcal{G}(\beta)}{G_c^{\text{int}}} & \rightarrow \text{penetration} \end{cases} . \tag{17}$$

Using Figure 6b, we can determine this graphically. Given an interface angle β and fracture toughness G_c^{int}, if the point corresponding to $\left(\beta, G_c^{\text{int}}/G_c^{\text{bulk}}\right)$ falls below the He and Hutchinson criterion Equation 15, then the fracture deflects; otherwise, the fracture penetrates.

4. Results

4.1. Energy Release Rates of a Deflecting Fracture

To examine how energy release rates change with the distance from the wellbore, we computed the energy release rates of penetrating and deflecting fractures at a grain boundary in our experimental setting. In a half-domain of the sample in plane strain, we considered a straight hydraulic fracture arriving at the center of a grain located at a distance d away from the wellbore (Figure 7). Because the fluid viscosity was low (0.8 mPa·s) and the fracture scale was small (~6 mm), we neglected the pressure loss within the fracture and applied the same hydraulic pressure (15 MPa) to the wellbore's internal wall and the fracture surfaces. Because all mineral grains were calcite, Young's modulus and Poisson's ratio of the inclusion were considered identical to those of the bulk rock. Table 1
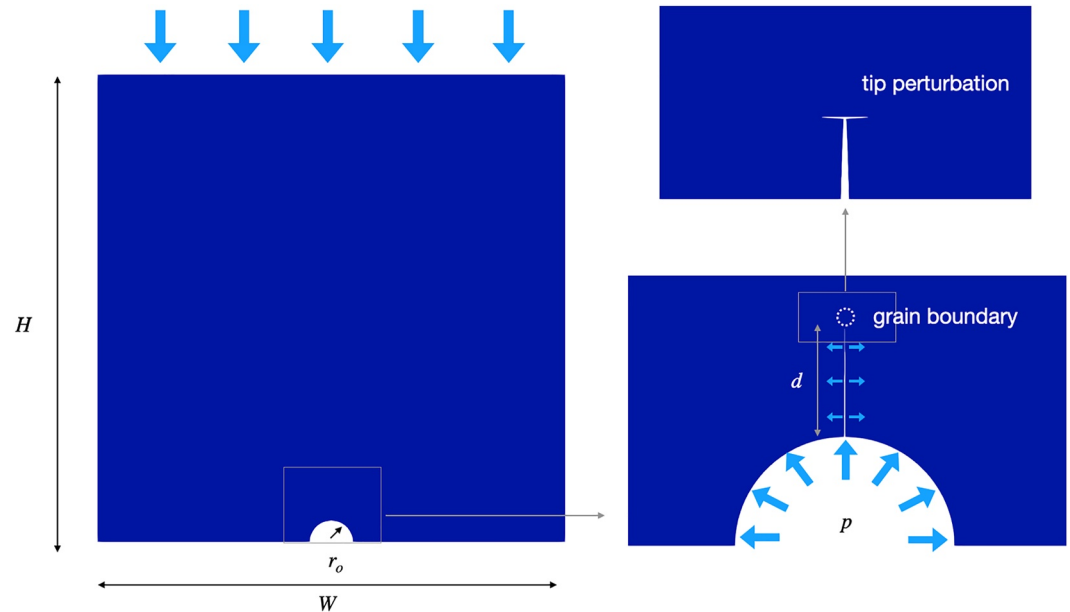
Figure 7. Energy release rate computation for a half-domain of the sample in 2D plane strain for $d = r_o$. A loading of 5 MPa is applied from the top, and the borehole and the crack are internally pressurized at 15 MPa. The fracture reaches a grain located at d and is deflected by 90°, splitting its tip into two (schematic).

lists the physical and geometrical parameters used in the analyses. All the parameters were taken from Naoi et al. (2020) except for the fracture toughness, which was not measured, and we used a typical fracture toughness value for carbonates (10 Pa·m). The inclusion radius (0.1 mm) is a typical size observed in the samples.

In the absence of an analytical expression for this particular setting, we numerically approximated energy release rates Equation 2 as,

$$\mathcal{G} = -\frac{\partial \Pi}{\partial l} \approx -\frac{\Delta \Pi}{\Delta l}. \tag{18}$$

We perturbed the crack tip by a small increment (Δl), and then computed the corresponding potential energy (Π) at each increment. To represent a penetrating crack, we extended the tip straight, and for a deflecting crack, we extended the tip by splitting it into two tips deflected by 90° in opposite directions (Figure 7) (see Appendix B for the computational details and verification examples).

In accordance with the deflection/penetration criteria in Figure 6, we normalized the energy release rates of a deflecting fracture ($\mathcal{G}_d$) against the energy release rate of a penetrating fracture ($\mathcal{G}_p$). This normalized energy release rate represents the likelihood of fracture deflection; the higher it is, the more likely a fracture deflects for the same fracture toughness. Figure 8 plots the normalized energy release rates against the normalized distance from the wellbore (d/r_o). The energy release, or the likelihood, increases with the distance from the borehole. Recalling the relationship between energy release rate and stress intensity factor Equation 8, this trend is equivalent to an increase in stress intensity factors with the distance. This increasing trend continues to about twice the wellbore radius ($d/r_o \sim 2$).

4.2. Simulation of Hydraulic Fracture Interactions at a Grain Boundary

To examine the effect of grain boundary strength and location on hydraulic fracture behavior, we simulated the propagation of a hydraulic fracture and its interaction with a mineral grain using a variational phase-field model (Bourdin et al., 2012). The model is based on minimization of the

Table 1
Material Properties and Geometrical and Loading Parameters

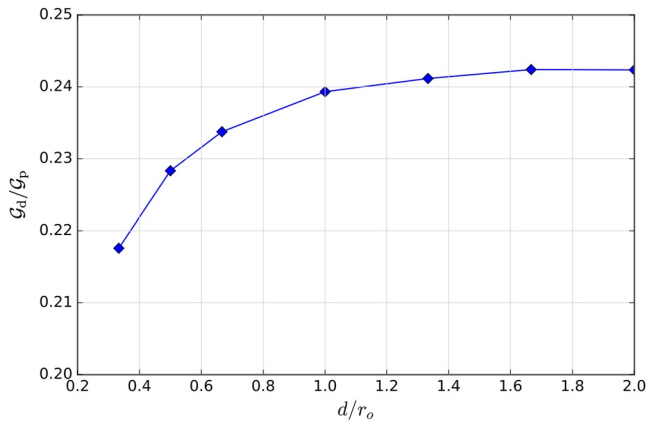| Name	Symbol	Value	Unit
Young's modulus	E	50	GPa
Fracture toughness of bulk	G_c^{bulk}	10	Pa·m
Poisson's ratio	ν	0.33	–
Axial loading	–	5	MPa
Wellbore pressure	–	15	MPa
Width	W	65	mm
Height	H	65	mm
Wellbore radius	r_o	3	mm
Inclusion radius	–	0.1	mm

Figure 8. Energy release rate of a deflecting crack normalized by that of a penetrating crack $\mathcal{G}_d/\mathcal{G}_p$ plotted against the normalized distance from the wellbore d/r_o. The symbols represent energy release rates at $d = 1/3r_o$, $1/2r_o$, $2/3r_o$, r_o, $4/3r_o$, $5/3r_o$, and $2r_o$.

Francfort-Marigo energy Equation 4 with phase-field regularization. Details are given in Appendix C.

Again, given the low fluid viscosity and small fracture scale, we neglected pressure loss within fractures. Furthermore, because of the low sample permeability (around 1 nanodarcy, see Supporting Information S1), we neglected fluid leak-off to and poro-elastic deformation in the rock formation. The injection rate was set at 1 cc min^{-1}. (Because pressure loss and leak-off are ignored, the injection rate is simply the fracture volume increase in one time step and has no other physical impact.) A mineral grain was placed at a distance d from the wellbore and, for numerical simplicity, a short fracture, $\Gamma = \{0\} \times [r, r + 0.25d]$, was prescribed. We represented the grain boundary by assigning a weaker fracture toughness to the interface than that of the bulk rock (i.e., $G_c^{int} < G_c^{bulk}$) while keeping their elastic properties identical.

We considered three different fracture toughnesses at the grain boundary: strong $\left(G_c^{int} = 0.2G_c^{bulk}\right)$, moderate $\left(G_c^{int} = 0.1G_c^{bulk}\right)$, and weak $\left(G_c^{int} = 0.05G_c^{bulk}\right)$. We also considered three different grain positions relative to the wellbore: near ($d = 1/3r_o$), middle ($d = 2/3r_o$), and far ($d = 3/3r_o$). Our simulations show that the fracture penetrates the grain without deflecting at the grain boundary for all toughness cases if the grain is in the near position (Figure 9a). With the grain in the middle position (Figure 9b), the fracture deflects in the weak boundary toughness case, but not in the other cases. With the grain in the far position (Figure 9c), the fracture deflects in the moderate and weak cases, but not in the strong case.

5. Discussion

Our work shows that the energy release rate of a deflecting fracture increases with the distance from the wellbore, which means that the farther a fracture propagates away from the wellbore, the more likely it is to deflect at a defect in the rock mass. According to our analysis, the likelihood of fracture deflection continues to increase up to about twice the wellbore radius ($2r_o$) if all other things are equal (Figure 8). Because grains and defects in real rocks are not distributed uniformly and their boundary toughnesses vary, our experiments exhibited varying degrees of complexity, but deflections peaked somewhere between $d/r_o = 0.5$ and $d/r_o = 2$ (Figure 5b), a result remarkably close to our analysis. Simulations with various grain locations and boundary toughnesses confirmed two things: (a) for grains at a given distance, the fracture deflects more easily at a weaker grain boundary, and (b) for grains with the same boundary toughness, the fracture deflects more easily at a grain more distant from the wellbore.

The first claim seems intuitive, but the second may not. To rationalize the second claim, let us consider the disturbance that the fluid pressure imposes on the stress field. Fluid pressure acts on both the wellbore walls and the fracture surfaces. While the fluid pressure inside the fracture imposes a tensile loading at the crack tip, the fluid pressure on the wellbore induces a loading parallel to the main fracture as depicted in Figure 7. This parallel loading to the propagation direction then suppresses the tendency of the fracture to deviate from the propagation direction. Considering Kirsch's solution in an infinite domain under uniaxial loading of σ_H (Kirsch, 1898) and Lame's solution for an infinitely thick wall cylinder (Timoshenko & Goodier, 1970, p. 69), the radial stress in the direction parallel to σ_H is,

$$\sigma_r = \frac{\sigma_H}{2}\left(1 - \frac{r_o^2}{r^2}\right) + \frac{\sigma_H}{2}\left(1 - \frac{r_o^2}{r^2}\right)\left(1 - \frac{3r_o^2}{r^2}\right) + p_w\frac{r_o^2}{r^2}, \tag{19}$$

where p_w is the wellbore pressure. The radial stress σ_r acts against the fracture deflection near the fracture tip. In accordance with our analysis and experiment, let us set $p_w = 3\sigma_H$ ($p_w = 15$ MPa, $\sigma_H = 5$ MPa). Then we have

$$\frac{\sigma_r}{p_w} = \frac{1}{2} + \frac{1}{6}\left(\frac{r_o}{r}\right)^2 + \frac{1}{2}\left(\frac{r_o}{r}\right)^4. \tag{20}$$

The formulation in Equation 20 shows that the radial stress σ_r decreases rapidly with the distance from the wellbore; from the wellbore $r = r_o$ ($d = 0$) to $r = 3r_o$ ($d = 2r_o$), the normalized radial stress (σ_r/p_w) drops by 60%. Thus,
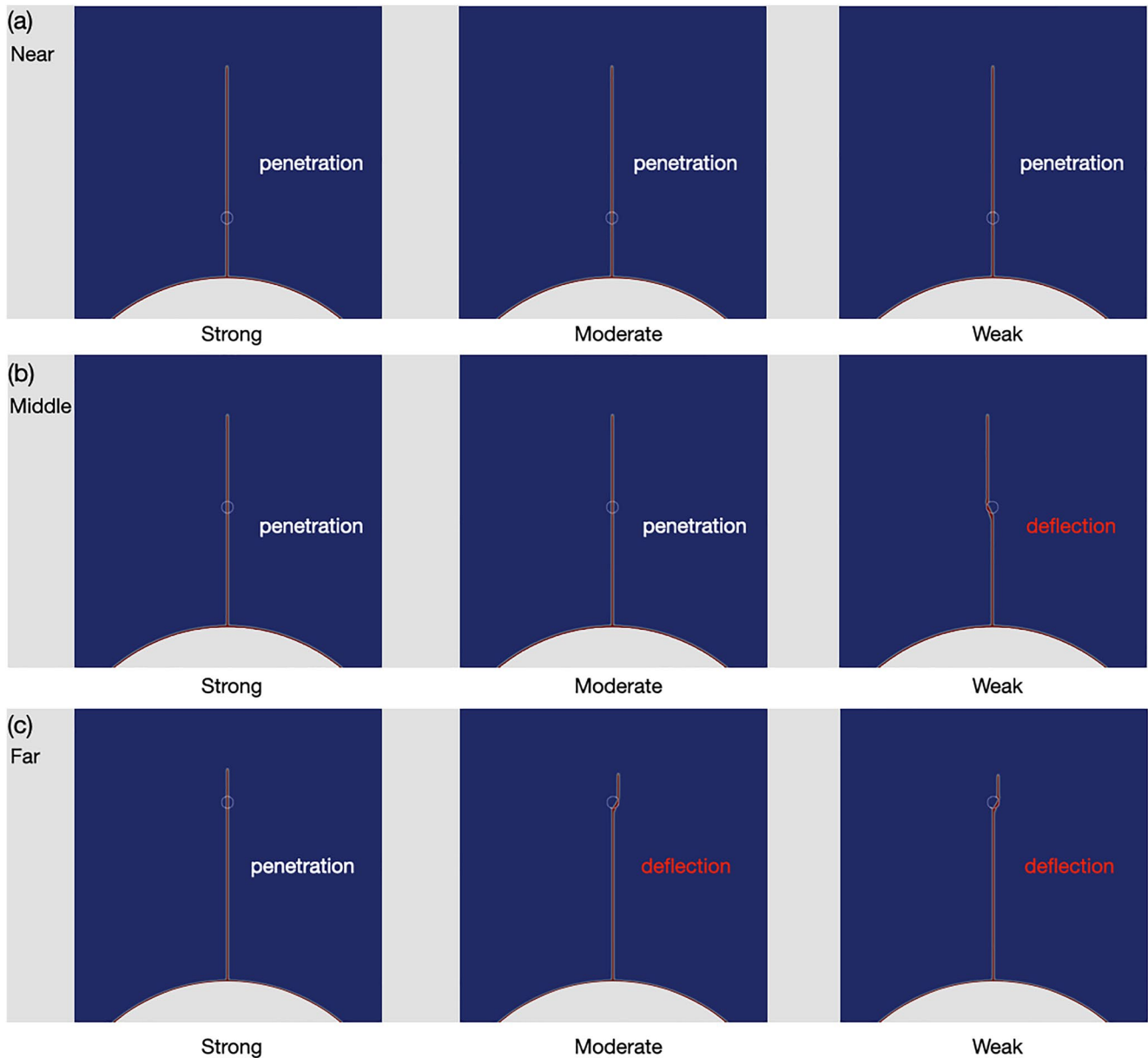
Figure 9. Phase-field simulation results with a grain position of (a) near $d = 1/3r_o$, (b) middle $d = 2/3r_o$, and (c) far $d = r_o$. For each cases, three different interface fracture toughnesses were simulated (strong $G_c^{int} = 0.2G_c^{bulk}$, moderate $G_c^{int} = 0.1G_c^{bulk}$, and weak $G_c^{int} = 0.05G_c^{bulk}$.

a fracture will be less suppressed against deflection as it propagates farther from the wellbore. This is an overly simplified analysis of our experiments ignoring the finite domain and pressurized fractures, but it helps understand the implications of our energy release rate analyses. We also note that a rigorous analysis of stresses around the fracture tip with a discontinuity is a daunting and, unfortunately, futile effort because approaches based on stress intensity factors will fall short of predicting the fracture path in anisotropic or heterogeneous media, as discussed in Section 3.3.

Most previous studies of fracture propagation criteria have focused on the interplay between the in situ stress and the geometry and strength of natural fractures. However, our study demonstrates that the presence of a pressurized wellbore appreciably affects the fracture interactions with grain boundary discontinuities in the near wellbore region. Although the pressurized wellbore impact has been considered in the past in the context of tortuous fracture propagation when a fracture is initiated in a direction not orthogonal to the minimum in situ stress (Feng & Gray, 2018; X. Zhang et al., 2011), to the best of our knowledge, this study is the first to consider the effects

of pressurized wellbore on fracture penetration/deflection at a grain boundary discontinuity in the near wellbore region. Our findings also underscore that analysis should address not only the local stress stability around the fracture tip but also the global energetic field which takes into account the presence of other fractures or a wellbore. Thus, we would caution against uncritically transferring criteria for fracture deflection/penetration from one setting to another, especially when other wells or fractures are present.

Our energy release rate analyses in Section 4.1 are based on linear elastic fracture mechanics, which is applied to describe fracture propagation in a wide range of scale sizes from 10^{-6} m (Shimada et al., 2015) to 10^2 m (Detournay, 2016). At our experimental scale, a grain boundary acts as a discontinuity. At larger scales, however, discontinuities may be defects in the rock mass or preexisting fractures, and our findings on near wellbore fracture behaviors may apply not just to grain boundaries, but to these discontinuities as well. We also note that our analysis considered a pressurized wellbore, which is applicable to open-hole completions but does not apply to cased and perforated completions, in which the casing will prevent the wellbore pressure force from directly acting on the rock formation. However, if the cementing of the casing is not perfect, then seeping fluid may pressurize the interface between the cement and the rock formation, bringing the conditions closer to those of this study. Conversely, if a rock–cement interface is tightly sealed, induced fractures will likely interact more strongly with grain boundary discontinuities in the near wellbore region shown in Figure 8 ($d = 2r_o$). Alternatively, if perforations extend past $d = 2r_o$, then fractures issuing from the perforations may become complex. Both situations should increase the fracture complexity immediately around the wellbore and result in improved well productivity.

Among all the fractures analyzed (Figure 4), the upper fracture in sample # 1 exhibits a much greater normalized length (∼4.5) than the others. In terms of the mineral grain distribution, we did not observe anything particular compared to the other samples. On the other hand, the recorded breakdown pressure of sample #1 was higher (11.09 MPa) than the other 2 samples (10.30 and 10.71 MPa). One possible explanation for the high degree of complexity is that the rock mass had a higher fracture toughness and induced a higher breakdown pressure which led to faster fracture propagation. This then may have caused more unstable and more complex fracture propagation. To investigate this claim, however, dynamic fracture mechanics needs to be considered and may be a topic of future study.

Furthermore, in this study, we focused only on the very first deflection of a fracture, when a straight fracture arrives at a grain boundary discontinuity. Fracture interactions with discontinuities after the first deflection (non-straight fracture) may be important subjects for future studies. Additionally, we did not consider fluid effects, although we can no longer neglect pressure loss within the fracture or fluid leak-off to the rock formation under some circumstances. For example, experimental studies have reported increasing hydraulic fracture complexities with the use of a low–viscosity fluid (Ishida et al., 2016; Watanabe et al., 2017). These effects too should be considered in future studies.

6. Conclusions

We have studied a phenomenon repeatedly observed in our hydraulic fracturing experiments: the increasing tendency of fracture deflection with the distance from the wellbore. We were able to quantitatively explain this increasing complexity through an analysis on the energy release rates. Our numerical simulation results also report an increasing likelihood of fracture deflection at grain boundaries with the distance from the wellbore. Both computations were based on energy minimization and agreed with our experimental observations. From these findings, we conclude that fracture paths are better determined on the basis of global energy dissipation rather than local stresses around the fracture tip, especially in anisotropic or heterogeneous formations.

Appendix A: Fracture Path Quantification

From the thin section images (Figure 3), we determined the fracture paths and lengths as follows (Figure 4):

1. Register the main and branch fractures in sequences of pixels.
2. Set the beginning of the main fracture as the origin and assign the pixels to Cartesian coordinates (x_j, y_j) by multiplying them by the image resolution (2.2 μm).
3. Compute the overall propagation direction vector for the main fracture, $\mathbf{w} = (\cos\theta, \sin\theta)$, by the least squares method, that is,

$$\tan \theta = \frac{\sum_{i=1}^{N} x_i y_i}{\sum_{i=1}^{N} x_i^2},$$

where $(x_1, y_1) = \mathbf{0}$ and N corresponds to the point when $\sqrt{x_N^2 + y_N^2}$ equals the end of the image (18 mm).

4 In each 10 μm interval along the propagation direction $\mathbf{w}$, compute the discrete fracture length l_j assuming that the fractures are linear within each interval.
5 Integrate the discrete fracture lengths as

$$L = \sum_{j} l_j.$$

Steps 2–5 were repeated for L_m and L_t except that the propagation directions (θ in step 3) were only calculated for the main fractures.

Appendix B: Numerical Energy Release Rate Analysis

For computation of energy release rates, several integral-based approaches are available such as J-integral (Rice, 1968) or the G_θ method (Dubois et al., 1998). However, for non–smooth deflection (kinking), these methods do not appear to compute the energy release rate accurately, even with reasonable element refinement. Therefore, we approximated the energy release rates using Equation 18 by evaluating potential energies from a linear elastic finite element analysis with perturbations in the fracture length.
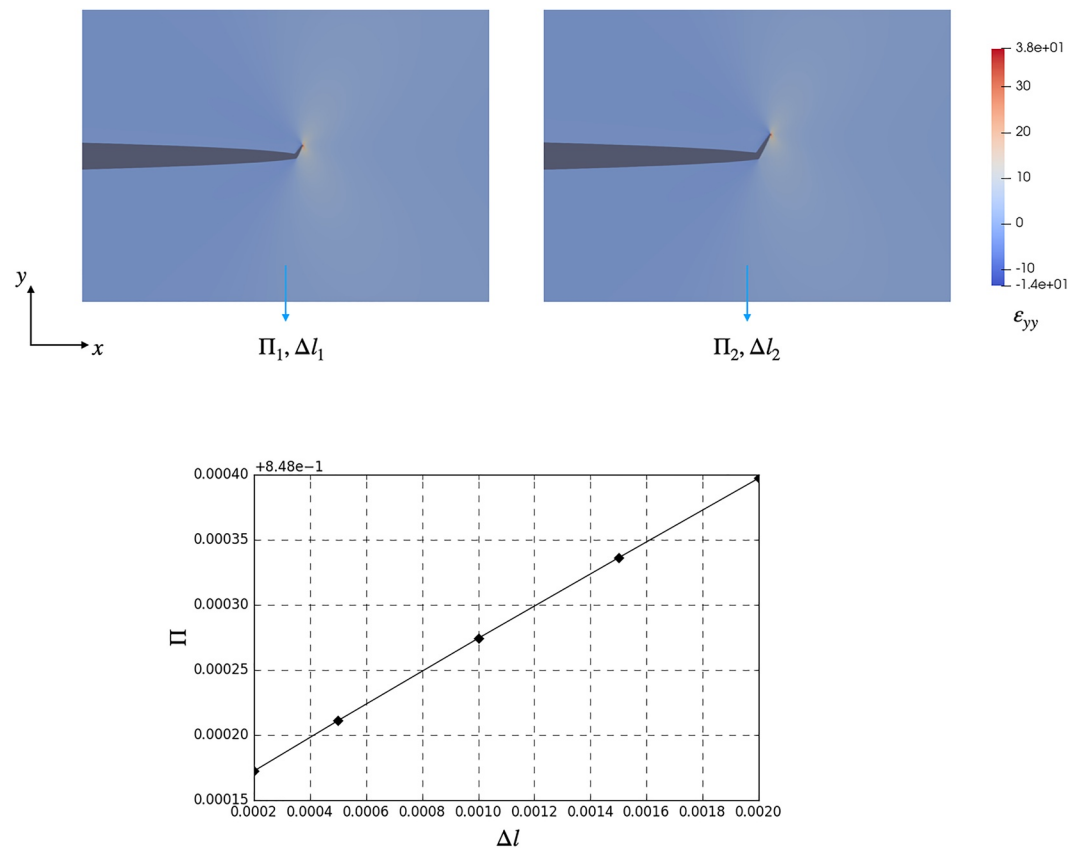

Figure B1. Example of the computation of an energy release rate. The top figures show computed deformation (colored with the strain in the y-direction) with different crack tip perturbations. For each configuration, we computed the potential energies and plotted them against the fracture tip growth. The slope of the resulting line gives the energy release rate (bottom).
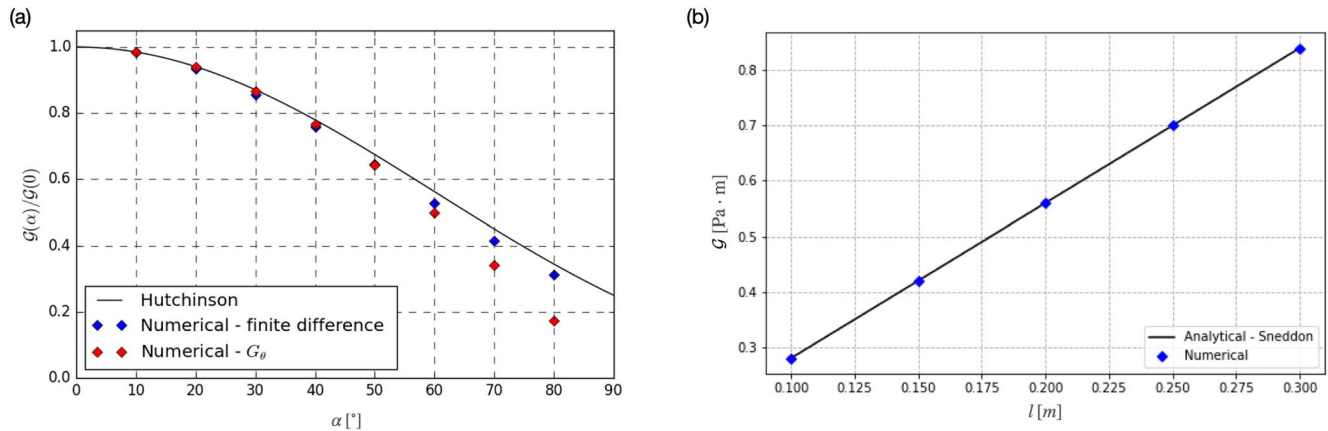
Figure B2. Comparisons of the computation of an energy release rates with results from the solutions of (a) He and Hutchinson (1989) and (b) Sneddon and Lowengrub (1969).

Theoretically, we can estimate $\mathcal{G}$ by running two linear elastic analyses with, say, Δl_1 and Δl_2 ($\Delta l_2 > \Delta l_1$) and computing the corresponding potential energies (Π_1 and Π_2) as:

$$\mathcal{G} \approx -\frac{\Pi_1 - \Pi_2}{\Delta l_1 - \Delta l_2}.$$

In this study, we computed the potential energy with five different fracture tip perturbation lengths for each geometrical configuration to ensure that (1) the perturbation of l is small enough and (2) the element discretization is adequate by checking whether the Π versus Δl curve falls on a straight line (Figure B1).

The potential energy is written according to the Clapeyron theorem (Fosdick & Truskinovsky, 2004) with stress $\boldsymbol{\sigma}$ and strain $\boldsymbol{\varepsilon}$ as

$$\Pi = \frac{1}{2}\int_\Omega \boldsymbol{\sigma} : \boldsymbol{\varepsilon}\, dx, \tag{B1}$$

where $\boldsymbol{\varepsilon}$ is the linearized strain $\left(\boldsymbol{\varepsilon} := 1/2\left(\nabla\mathbf{u} + \nabla\mathbf{u}^{\mathrm{T}}\right)\right)$ and $\mathbf{u}$ is the displacement. Figure B1 shows the computation of $\mathcal{G}$ for 80° fracture deflection in the He and Hutchinson problem (Figure 6a).

To verify our computational procedure for $\mathcal{G}$, we compared the numerically obtained values of $\mathcal{G}(\alpha)/\mathcal{G}(0)$ with the analytical expression of He and Hutchinson (1989) in Figure B2a. The energy release rates computed with the G_θ method are also plotted. Both approaches follow a similar decreasing trend, but as the deflection angle grows, the G_θ method deviates from the analytical expression.

Furthermore, we verified computations of the absolute $\mathcal{G}$ value for a line fracture ($[-a, +a] \times \{0\}$) pressurized by a constant pressure, p, in an infinite domain. Sneddon and Lowengrub (1969) derived an analytical solution to this problem:

$$\mathcal{G} = \frac{p^2 \pi l}{E'}.$$

The computed energy release rates are in close agreement with the analytical solution with various fracture lengths (Figure B2b).

Appendix C: A Variational Phase-Field Model for Hydraulic Fracture

C1. A Variational Phase-Field Model for Fracture

Although the Griffith criterion is presented in a generalized form in Equation 4, its numerical implementation is not straightforward because of the discontinuous and evolving crack set Γ. Among available methods (Schmidt et al., 2009; Wang & Sun, 2017), a regularization method via Gamma-convergence (Bourdin et al., 2000;

Chambolle, 2004) has become the standard implementation method for Equation 4 in the last decade (e.g., Ambati et al., 2014; Borden et al., 2012; Freddi & Royer-Carfagni, 2010) and is now typically referred to as the phase-field model.

Following Bourdin et al. (2000), we introduce a scalar phase-field variable, $v : \Omega \mapsto [0, 1]$ and a regularization length parameter $\ell > 0$. Then the total energy $\mathcal{E}_\ell$ (Bourdin et al., 2014; Pham et al., 2011) is approximated by

$$\mathcal{E}_\ell = \frac{1}{2} \int_\Omega v^2 \boldsymbol{\sigma} : \boldsymbol{\varepsilon} \, d\Omega + \int_\Omega \frac{3G_c}{8} \left(\frac{1-v}{\ell} + \ell |\nabla v|^2 \right) d\Omega. \tag{C1}$$

The minimization problem now reads:

$$(\mathbf{u}, v) = \arg\min_{\mathbf{u}, v} \mathcal{E}_\ell(\mathbf{u}, v). \tag{C2}$$

The approximated energy functional Equation C1 converges to Equation 5 as $\ell \to 0$ in the sense of Gamma-convergence, meaning that the minimizers of Equation C1, $(\mathbf{u}, v)$, converge to those of Equation 5, $(\mathbf{u}, \Gamma)$, as $\ell \to 0$.

C2. Extension to Hydraulic Fracturing

To extend Equation C1 to hydraulic fracturing, we need to account for the work by fluid pressure forces on the fracture surfaces (Bourdin et al., 2012)

$$\int_\Gamma p_f [\![\mathbf{u} \cdot \mathbf{n}]\!] \, d\Gamma,$$

where $[\![\cdot]\!]$ expresses the jump quantity, p_f is the fluid pressure in the fracture and $\mathbf{n}$ is the normal vector to the fracture surface Γ. Following Bourdin et al. (2012) and Chukwudozie et al. (2019), we can approximate it as

$$\int_\Gamma p_f [\![\mathbf{u} \cdot \mathbf{n}]\!] \, d\Gamma \approx \int_\Omega p_f \mathbf{u} \cdot \nabla v \, d\Omega.$$

The stress-strain relation is

$$\boldsymbol{\sigma} = \mathbb{C} : \boldsymbol{\varepsilon} - \alpha_B p_p \mathbf{I}, \tag{C3}$$

where $\mathbb{C}$ is the tangential stiffness tensor, p_p is the pore-pressure and α_B is Biot's coefficient. In this study, because of the tight permeability of the sample and the short duration of injection, we assumed no leak-off. Thus p_p is a temporary constant ($p_p(x, t) \to p_p(x)$). Additionally, because of the small sample size, the pressure loss within the fracture is negligible. Thus we assume that p_f is spatially uniform ($p_f(x, t) \to p_f(t)$) and the pore-pressure is ambient ($p_p(x) \to 0$). Denoting $p_f(t)$ with p, the regularized total energy now reads:

$$\mathcal{F}_\ell := \frac{1}{2} \int_\Omega v^2 \mathbb{C} : \boldsymbol{\varepsilon} : \boldsymbol{\varepsilon} \, d\Omega + \int_\Omega \frac{3G_c}{8} \left(\frac{1-v}{\ell} + \ell |\nabla v|^2 \right) d\Omega - p \int_\Omega \mathbf{u} \cdot \nabla v \, d\Omega. \tag{C4}$$

This model does not differentiate fracture evolution with respect to the sign of strain; that is, the fracture evolves identically under tension and compression (Amor et al., 2009). To avoid such unphysical behaviors, a number of different models that split the strain energy, the first term in Equation C4, have been proposed (Freddi & Royer-Carfagni, 2010; Miehe et al., 2010; Steinke & Kaliske, 2019; J.-Y. Wu, 2017). In this study, we adapted an approach proposed by Freddi and Royer-Carfagni (2010) in which the strain is split into positive and negative parts as

$$\boldsymbol{\varepsilon} = \boldsymbol{\varepsilon}_+ + \boldsymbol{\varepsilon}_-, \tag{C5}$$

where $\boldsymbol{\varepsilon}_+$ is a positive definite tensor that meets the following orthogonality condition (T. Li et al., 2016; Ziaei-Rad et al., 2023):

$$\mathbb{C} : \boldsymbol{\varepsilon}_+ : \boldsymbol{\varepsilon}_- = 0. \tag{C6}$$

With this split, we rewrite the first integrand so that only the positive part of the strain energy contributes to fracturing:

$$v^2 \mathbb{C} : \varepsilon : \varepsilon \to v^2 \mathbb{C} : \varepsilon_+ : \varepsilon_+ + \mathbb{C} : \varepsilon_- : \varepsilon_-. \tag{C7}$$

Equivalently, we can write

$$v^2 \mathbb{C} : \varepsilon_+ : \varepsilon_+ + \mathbb{C} : \varepsilon_- : \varepsilon_- = \left(v^2 \mathbb{C}_+ + \mathbb{C}_-\right) : \varepsilon : \varepsilon, \tag{C8}$$

where

$$\mathbb{C}_\pm = \frac{\partial^2}{\partial \varepsilon^2}\left(\frac{1}{2}\mathbb{C} : \varepsilon_\pm : \varepsilon_\pm\right). \tag{C9}$$

C3. Numerical Implementation

We control the injected volume in a quasi-static setting ($t = t_1, t_2, \ldots, t_n$) as $q = q_1, q_2, \ldots, q_n$. In this simplified setting or the so-called toughness dominated regime (Detournay, 2016), we can simply enforce mass conservation at time step i as

$$Q_i := \int_t q\, dt = V_i, \tag{C10}$$

where V_i is the fracture volume at time step i and is given as (Bourdin et al., 2012)

$$V_i = \int_\Omega \mathbf{u}_i \cdot \nabla v_i\, d\Omega. \tag{C11}$$

With this mass conservation constraint, our minimization problem Equation C4 now reads

$$(\mathbf{u}_i, v_i; p) = \arg \min_{\mathbf{u}, v}\left\{\mathcal{F}_\ell(\mathbf{u}, v; p) : \mathbf{u} \in \mathcal{U}(t_i), v \in \mathcal{V}(t_i, v_{i-1}), Q_i = \int_\Omega \mathbf{u}_i \cdot \nabla v_i\, d\Omega\right\}, \tag{C12}$$

where $\mathcal{U}$ is the kinematically admissible displacement set:

$$\mathcal{U}(t_i) = \left\{\mathbf{u} \in H^1(\Omega) : \mathbf{u} = 0 \quad \text{on} \quad \partial\Omega_D\right\}, \tag{C13}$$

and $H^1(\Omega)$ is a Sobolev space of order 1 on Ω. The kinematically admissible set of v requires the irreversible condition (Bourdin, 2007; Burke et al., 2013)

$$\mathcal{V}(t_i, v_{i-1}) = \left\{v \in H^1(\Omega) : 0 \leq v(x) \leq \eta\ \forall x\right\}, \tag{C14}$$

where

$$\eta = \begin{cases} 1 & \text{if} \quad v_{i-1}(x) \geq v_{ir} \\ v_{i-1}(x) & \text{otherwise} \end{cases}$$

and v_{ir} is the irreversible threshold $\in [0, 1]$ (e.g., 0.05).

The current implementation guarantees to find local minima by considering the first–order optimality condition

$$\mathcal{F}_\ell'(\mathbf{u}, v)(\tilde{\mathbf{u}}, \tilde{v}) \geq 0 \quad \forall(\tilde{\mathbf{u}}, \tilde{v}) \in \mathcal{U} \times \mathcal{V}, \tag{C15}$$

where $\mathcal{F}_\ell'(\mathbf{u}, v)(\tilde{\mathbf{u}}, \tilde{v})$ is the Gâteaux derivative of $\mathcal{E}_\ell$ at $(\mathbf{u}, v)$ in the direction of $(\tilde{\mathbf{u}}, \tilde{v})$ and is given by:

$$\begin{aligned} \mathcal{F}_\ell'(\mathbf{u}, v)(\tilde{\mathbf{u}}, \tilde{v}) &= \int_\Omega \mathbb{C}(v) : \varepsilon(\mathbf{u}) : \varepsilon(\tilde{\mathbf{u}})\, dV - \int_\Omega \mathbf{f} \cdot \tilde{\mathbf{u}}\, dV - \int_{\partial_N \Omega} \boldsymbol{\tau} \cdot \tilde{\mathbf{u}}\, dS - p \int_\Omega \tilde{\mathbf{u}} \cdot \nabla v\, dV \\ &\quad + \int_\Omega 2v\tilde{v}\psi_+\, dV + \frac{1}{4c_n}\int_\Omega G_c\left(\frac{w'(v)}{\ell}\tilde{v} + 2\ell \nabla v \cdot \nabla \tilde{v}\right)dV - p \int_\Omega \mathbf{u} \cdot \nabla \tilde{v}\, dV, \end{aligned} \tag{C16}$$
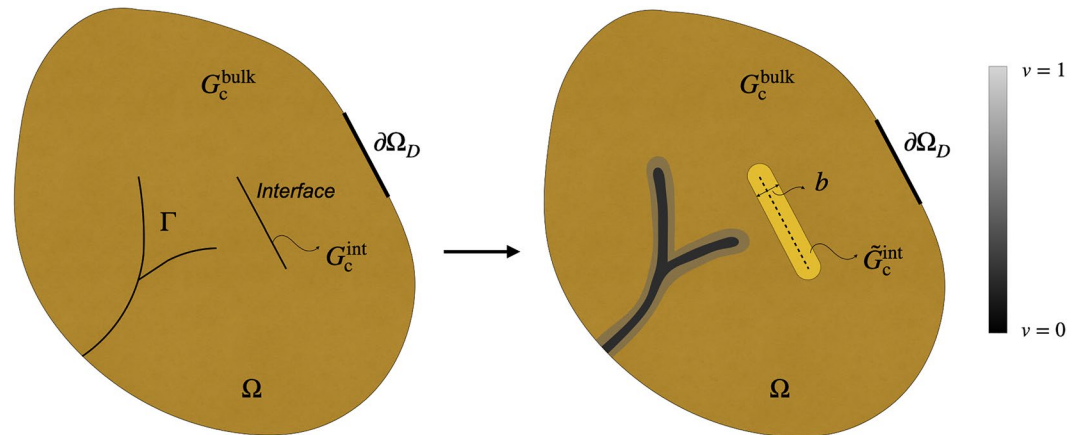
Figure C1. Diagram of a discontinuous interface and a crack set Γ in the sharp (left) and diffused (right) representations.

where $\mathbb{C}(v) = v^2\mathbb{C}_+ + \mathbb{C}_-$.

The minimization is performed via an alternate minimization scheme (Bourdin et al., 2000), taking advantage of the convexity of $\mathcal{F}_\ell$ with respect to **u** and v. $\mathcal{F}_\ell$ is first minimized with respect to **u** while fixing v and then minimized with respect to v while fixing **u** with the irreversible condition. As the solution for v requires an inequality constraint, $0 \leq v \leq \eta$, we employed a variational inequality solver from the PETSc library (Balay, Abhyankar, Adams, Benson, et al., 2020; Balay, Abhyankar, Adams, Brown, 2020).

C4. Interface Model

Interfaces such as a grain boundary occupy negligible physical space, and thus it is challenging to account for their presence in numerical simulations. We follow an approach proposed by Hansen-Dörr et al. (2019, 2020) and Yoshioka et al. (2021) in which an interface is numerically diffused over a certain length b (Figure C1). Within the diffused zone, the material posses an *effective* interface fracture toughness and outside of the diffused zone it posses the bulk fracture toughness. Toughness profiles in the sharp and diffused interface representations are presented in Figure C2.

We can estimate the effective fracture toughness $\tilde{G}_c^{\text{int}}$ by equating the energies from the sharp and diffused representations. In the sharp representation, the fracture surface energy is $G_c^{\text{int}} \int_\Gamma \mathrm{d}\Gamma$. This is diffused using the effective fracture toughness $\tilde{G}_c^{\text{int}}$:

$$G_c^{\text{int}} \int_{\Gamma_I} \mathrm{d}\Gamma = \tilde{G}_c^{\text{int}} \int_{\xi < b} S(v, \nabla v)\,\mathrm{d}\Omega + G_c^{\text{bulk}} \int_{\xi > b} S(v, \nabla v)\,\mathrm{d}\Omega, \tag{C17}$$
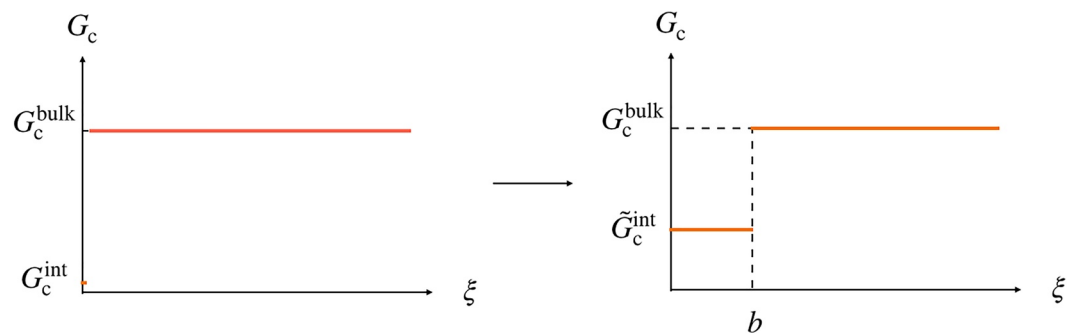

Figure C2. Fracture toughness profiles in (a) the sharp representation and (b) the diffused representation of the interface, in which the effective toughness is assigned over the subdomain $\xi < b$.

where ξ is the shortest distance from the interface and

$$S(v, \nabla v) := \frac{3}{8}\left(\frac{1-v}{\ell} + \ell|\nabla v|^2\right).$$ (C18)

In earlier work (Yoshioka et al., 2021), Equation C17 was solved analytically in 1D and verified numerically in 2D and 3D. In this study, we computed G_c profiles from the interface toughness G_c^{int} and the toughness of bulk rock, G_c^{bulk}.

Data Availability Statement

The hydraulic fracturing simulations were performed by an open-source code, OpenGeoSys, which can be freely downloaded at https://www.opengeosys.org. The simulation input files, the output results, and the scripts used for the energy release computations are available at https://doi.org/10.5281/zenodo.6390977 (Yoshioka, 2022). The pressure and acoustic emission recordings, and the original used for analyses are available at https://doi.org/10.5281/zenodo.6811452 (Yoshioka et al., 2022).

References

Abou-Sayed, A., Brechtel, C., & Clifton, R. (1978). In situ stress determination by hydrofracturing: A fracture mechanics approach. *Journal of Geophysical Research*, *83*(B6), 2851–2862. https://doi.org/10.1029/jb083ib06p02851

Ambati, M., Gerasimov, T., & De Lorenzis, L. (2014). A review on phase-field models of brittle fracture and a new fast hybrid formulation. *Computational Mechanics*, *55*(2), 383–405. https://doi.org/10.1007/s00466-014-1109-y

Amestoy, M., & Leblond, J. (1992). Crack paths in plane situations–II: Detailed form of the expansion of the stress intensity factors. *International Journal of Solids and Structures*, *29*(4), 465–501. https://doi.org/10.1016/0020-7683(92)90210-k

Amor, H., Marigo, J.-J., & Maurini, C. (2009). Regularized formulation of the variational brittle fracture with unilateral contact: Numerical experiments. *Journal of the Mechanics and Physics of Solids*, *57*(8), 1209–1229. https://doi.org/10.1016/j.jmps.2009.04.011

Anderson, T. (1995). *Fracture mechanics* (2nd ed.). CRC Press.

Balay, S., Abhyankar, S., Adams, M. F., Benson, S., Brown, J., Brune, P., et al. (2020). *PETSc/TAO users manual (Technical Report No. ANL-21/39—Revision 3.16)*. Argonne National Laboratory.

Balay, S., Abhyankar, S., Adams, M. F., Brown, J., Brune, P., Buschelman, K., et al. (2020). PETSc web page.

Baumgärtner, J., & Zoback, M. (1989). Interpretation of hydraulic fracturing pressure-time records using interactive analysis methods. *International Journal of Rock Mechanics and Mining Sciences & Geomechanics Abstracts*, *26*(6), 461–469. https://doi.org/10.1016/0148-9062(89)91422-8

Blanton, T. L. (1982). An experimental study of interaction between hydraulically induced and pre-existing fractures. In *SPE unconventional gas recovery symposium*.

Borden, M., Verhoosel, C., Scott, M., Hughes, T., & Landis, C. (2012). A phase-field description of dynamic brittle fracture. *Computer Methods in Applied Mechanics and Engineering*, *217–220*, 77–95. https://doi.org/10.1016/j.cma.2012.01.008

Bourdin, B. (2007). Numerical implementation of the variational formulation for quasi-static brittle fracture. *Interfaces and Free Boundaries*, *9*(3), 411–430. https://doi.org/10.4171/ifb/171

Bourdin, B., Chukwudozie, C., & Yoshioka, K. (2012). A variational approach to the numerical simulation of hydraulic fracturing. In *SPE annual technical conference and exhibition*.

Bourdin, B., Francfort, G., & Marigo, J.-J. (2000). Numerical experiments in revisited brittle fracture. *Journal of the Mechanics and Physics of Solids*, *48*(4), 797–826. https://doi.org/10.1016/s0022-5096(99)00028-9

Bourdin, B., Marigo, J. J., Maurini, C., & Sicsic, P. (2014). Morphogenesis and propagation of complex cracks induced by thermal shocks. *Physical Review Letters*, *112*(1), 1–5. https://doi.org/10.1103/physrevlett.112.014301

Brach, S., Hossain, M., Bourdin, B., & Bhattacharya, K. (2019). Anisotropy of the effective toughness of layered media. *Journal of the Mechanics and Physics of Solids*, *131*, 96–111. https://doi.org/10.1016/j.jmps.2019.06.021

Bröker, K., & Ma, X. (2022). Estimating the least principal stress in a granitic rock mass: Systematic mini-frac tests and elaborated pressure transient analysis. *Rock Mechanics and Rock Engineering*, *55*(4), 1931–1954. https://doi.org/10.1007/s00603-021-02743-1

Burke, S., Ortner, C., & Süli, E. (2013). An adaptive finite element approximation of a generalized Ambrosio–Tortorelli functional. *Mathematical Models and Methods in Applied Sciences*, *23*(09), 1663–1697. https://doi.org/10.1142/s021820251350019x

Chambolle, A. (2004). An approximation result for special functions with bounded deformation. *Journal de mathématiques pures et appliquées*, *83*(7), 929–954. https://doi.org/10.1016/j.matpur.2004.02.004

Chambolle, A., Francfort, G. A., & Marigo, J.-J. (2009). When and how do cracks propagate? *Journal of the Mechanics and Physics of Solids*, *57*(9), 1614–1622. https://doi.org/10.1016/j.jmps.2009.05.009

Chen, Y., Nagaya, Y., & Ishida, T. (2015). Observations of fractures induced by hydraulic fracturing in anisotropic granite. *Rock Mechanics and Rock Engineering*, *48*(4), 1455–1461. https://doi.org/10.1007/s00603-015-0727-9

Chen, Y., Naoi, M., Tomonaga, Y., Akai, T., Tanaka, H., Takagi, S., & Ishida, T. (2018). Method for visualizing fractures induced by laboratory-based hydraulic fracturing and its application to shale samples. *Energies*, *11*(8), 1976. https://doi.org/10.3390/en11081976

Chukwudozie, C., Bourdin, B., & Yoshioka, K. (2019). A variational phase-field model for hydraulic fracturing in porous media. *Computer Methods in Applied Mechanics and Engineering*, *347*, 957–982. https://doi.org/10.1016/j.cma.2018.12.037

Chuprakov, D., Melchaeva, O., & Prioul, R. (2014). Injection-sensitive mechanics of hydraulic fracture interaction with discontinuities. *Rock Mechanics and Rock Engineering*, *47*(5), 1625–1640. https://doi.org/10.1007/s00603-014-0596-7

Ciezobka, J., Courtier, J., & Wicker, J. (2018). Hydraulic fracturing test site (HFTS)-project overview and summary of results. In *SPE/AAPG/SEG unconventional resources technology conference*.

Cipolla, C. L., Warpinski, N. R., Mayerhofer, M. J., Lolon, E., & Vincent, M. C. (2008). The relationship between fracture complexity, reservoir properties, and fracture treatment design. In *SPE annual technical conference and exhibition*.

Cladouhos, T. T., Petty, S., Swyer, M. W., Uddenberg, M. E., Grasso, K., & Nordin, Y. (2016). Results from newberry volcano EGS demonstration, 2010–2014. *Geothermics*, *63*, 44–61. https://doi.org/10.1016/j.geothermics.2015.08.009

Cotterell, B., & Rice, J. (1980). Slightly curved or kinked cracks. *International Journal of Fracture*, *16*(2), 155–169. https://doi.org/10.1007/bf00012619

Cuenot, N., Dorbath, C., & Dorbath, L. (2008). Analysis of the microseismicity induced by fluid injections at the EGS site of Soultz-sous-Forêts (Alsace, France): Implications for the characterization of the geothermal reservoir properties. *Pure and Applied Geophysics*, *165*(5), 797–828. https://doi.org/10.1007/s00024-008-0335-7

Dahi-Taleghani, A., Gonzalez, M., & Shojaei, A. (2016). Overview of numerical models for interactions between hydraulic fractures and natural fractures: Challenges and limitations. *Computers and Geotechnics*, *71*, 361–368. https://doi.org/10.1016/j.compgeo.2015.09.009

Dahi-Taleghani, A., & Olson, J. E. (2011). Numerical modeling of multistranded-hydraulic-fracture propagation: Accounting for the interaction between induced and natural fractures. *SPE Journal*, *16*(03), 575–581. https://doi.org/10.2118/124884-pa

Dahi-Taleghani, A., & Olson, J. E. (2014). How natural fractures could affect hydraulic-fracture geometry. *SPE Journal*, *19*(01), 161–171. https://doi.org/10.2118/167608-pa

Dehghan, A. N., Goshtasbi, K., Ahangari, K., & Jin, Y. (2015). The effect of natural fracture dip and strike on hydraulic fracture propagation. *International Journal of Rock Mechanics and Mining Sciences*, *75*, 210–215. https://doi.org/10.1016/j.ijrmms.2015.02.001

Detournay, E. (2016). Mechanics of hydraulic fractures. *Annual Review of Fluid Mechanics*, *48*(1), 311–339. https://doi.org/10.1146/annurev-fluid-010814-014736

Dubois, F., Chazal, C., & Petit, C. (1998). A finite element analysis of creep-crack growth in viscoelastic media. *Mechanics of Time-Dependent Materials*, *2*(3), 269–286. https://doi.org/10.1023/a:1009831400270

Fatahi, H., Hossain, M. M., & Sarmadivaleh, M. (2017). Numerical and experimental investigation of the interaction of natural and propagated hydraulic fracture. *Journal of Natural Gas Science and Engineering*, *37*, 409–424. https://doi.org/10.1016/j.jngse.2016.11.054

Feng, Y., & Gray, K. (2018). Modeling of curving hydraulic fracture propagation from a wellbore in a poroelastic medium. *Journal of Natural Gas Science and Engineering*, *53*, 83–93. https://doi.org/10.1016/j.jngse.2018.02.020

Fischer, T., Hainzl, S., Eisner, L., Shapiro, S. A., & Le Calvez, J. (2008). Microseismic signatures of hydraulic fracture growth in sediment formations: Observations and modeling. *Journal of Geophysical Research*, *113*(2), B02307. https://doi.org/10.1029/2007jb005070

Fosdick, R., & Truskinovsky, L. (2004). About Clapeyron's theorem in linear elasticity. In *The rational spirit in modern continuum mechanics* (pp. 399–426). Springer.

Francfort, G. A., & Marigo, J.-J. (1998). Revisiting brittle fracture as an energy minimization problem. *Journal of the Mechanics and Physics of Solids*, *46*(8), 1319–1342. https://doi.org/10.1016/s0022-5096(98)00034-9

Freddi, F., & Royer-Carfagni, G. (2010). Regularized variational theories of fracture: A unified approach. *Journal of the Mechanics and Physics of Solids*, *58*(8), 1154–1174. https://doi.org/10.1016/j.jmps.2010.02.010

Fu, W., Savitski, A. A., & Bunger, A. P. (2018). Analytical criterion predicting the impact of natural fracture strength, height and cemented portion on hydraulic fracture growth. *Engineering Fracture Mechanics*, *204*, 497–516. https://doi.org/10.1016/j.engfracmech.2018.10.002

Gol'dstein, R. V., & Salganik, R. L. (1974). Brittle fracture of solids with arbitrary cracks. *International Journal of Fracture*, *10*(4), 507–523. https://doi.org/10.1007/bf00155254

Griffith, A. A. (1921). VI. The phenomena of rupture and flow in solids. *Philosophical Transactions of the Royal Society of London-Series A: Containing Papers of a Mathematical or Physical Character*, *221*(582–593), 163–198.

Gu, H., Weng, X., Lund, J., Mack, M., Ganguly, U., & Suarez-Rivera, R. (2012). Hydraulic fracture crossing natural fracture at nonorthogonal angles: A criterion and its validation. *SPE Production & Operations*, *27*(01), 20–26. https://doi.org/10.2118/139984-pa

Guo, F., Morgenstern, N., & Scott, J. (1993). Interpretation of hydraulic fracturing pressure: A comparison of eight methods used to identify shut-in pressure. *International Journal of Rock Mechanics and Mining Sciences & Geomechanics Abstracts*, *30*(6), 627–631. https://doi.org/10.1016/0148-9062(93)91222-5

Guo, T., Zhang, S., Qu, Z., Zhou, T., Xiao, Y., & Gao, J. (2014). Experimental study of hydraulic fracturing for shale by stimulated reservoir volume. *Fuel*, *128*, 373–380. https://doi.org/10.1016/j.fuel.2014.03.029

Gurtin, M. E., & Podio-Guidugli, P. (1998). Configurational forces and a constitutive theory for crack propagation that allows for kinking and curving. *Journal of the Mechanics and Physics of Solids*, *46*(8), 1343–1378. https://doi.org/10.1016/s0022-5096(98)00002-7

Haimson, B., & Fairhurst, C. (1969). In situ stress determination at great depth by means of hydraulic fracturing. In *The 11th U.S. Symposium on rock mechanics (USRMS)*.

Hakim, V., & Karma, A. (2009). Laws of crack motion and phase-field models of fracture. *Journal of the Mechanics and Physics of Solids*, *57*(2), 342–368. https://doi.org/10.1016/j.jmps.2008.10.012

Hansen-Dörr, A. C., Dammaß, F., de Borst, R., & Kästner, M. (2020). Phase-field modeling of crack branching and deflection in heterogeneous media. *Engineering Fracture Mechanics*, *232*, 107004. https://doi.org/10.1016/j.engfracmech.2020.107004

Hansen-Dörr, A. C., de Borst, R., Hennig, P., & Kästner, M. (2019). Phase-field modelling of interface failure in brittle materials. *Computer Methods in Applied Mechanics and Engineering*, *346*, 25–42. https://doi.org/10.1016/j.cma.2018.11.020

Harrison, E., Kieschnick, W., & McGuire, W. (1954). The mechanics of fracture induction and extension. *Transactions of the AIME*, *201*(01), 252–263. https://doi.org/10.2118/318-g

He, M.-Y., & Hutchinson, J. W. (1989). Crack deflection at an interface between dissimilar elastic materials. *International Journal of Solids and Structures*, *25*(9), 1053–1067. https://doi.org/10.1016/0020-7683(89)90021-8

Howard, G. C., & Fast, C. (1950). Squeeze cementing operations. *Journal of Petroleum Technology*, *2*(02), 53–64. https://doi.org/10.2118/950053-g

Hubbert, M. K., & Willis, D. G. (1957). Mechanics of hydraulic fracturing. *Transactions of the AIME*, *210*(01), 153–168. https://doi.org/10.2118/686-g

Hussain, M., Pu, S., & Underwood, J. (1974). Strain energy release rate for a crack under combined mode I and mode II. In *Fracture analysis: Proceedings of the 1973 national symposium on fracture mechanics, part II*.

Hutchinson, J. W., & Suo, Z. (1991). Mixed mode cracking in layered materials. *Advances in Applied Mechanics*, *29*, 63–191.

Irwin, G. R. (1957). Analysis of stresses and strains near the end of a crack traversing a plate. *Journal of Applied Mechanics*, *24*(3), 361–364. https://doi.org/10.1115/1.4011547

Ishida, T., Chen, Y., Bennour, Z., Yamashita, H., Inui, S., Nagaya, Y., et al. (2016). Features of CO_2 fracturing deduced from acoustic emission and microscopy in laboratory experiments. *Journal of Geophysical Research: Solid Earth*, *121*(11), 8080–8098. https://doi.org/10.1002/2016jb013365

Jeffrey, R. G., Bunger, A. P., Lecampion, B., Zhang, X., Chen, Z. R., van As, A., et al. (2009). Measuring hydraulic fracture growth in naturally fractured rock. In *SPE annual technical conference and exhibition*.

Jeffrey, R. G., & Weber, C. (1994). Hydraulic fracturing experiments in the great northern coal seam. In *SPE Asia Pacific oil and gas conference and exhibition*.

Jung, H., Sharma, M. M., Cramer, D. D., Oakes, S., & McClure, M. W. (2016). Re-examining interpretations of non-ideal behavior during diagnostic fracture injection tests. *Journal of Petroleum Science and Engineering*, *145*, 114–136. https://doi.org/10.1016/j.petrol.2016.03.016

Kamali, A., & Ghassemi, A. (2019). DFIT considering complex interactions of hydraulic and natural fractures. In *SPE hydraulic fracturing technology conference and exhibition*.

Kirsch, C. (1898). Die theorie der elastizitat und die bedurfnisse der festigkeitslehre. *Zeitschrift des Vereines Deutscher Ingenieure*, *42*, 797–807.

Kraft, T., & Deichmann, N. (2014). High-precision relocation and focal mechanism of the injection-induced seismicity at the Basel EGS. *Geothermics*, *52*, 59–73. https://doi.org/10.1016/j.geothermics.2014.05.014

Lamont, N., & Jessen, F. (1963). The effects of existing fractures in rocks on the extension of hydraulic fractures. *Journal of Petroleum Technology*, *15*(02), 203–209. https://doi.org/10.2118/419-pa

Lecampion, B., Bunger, A., & Zhang, X. (2018). Numerical methods for hydraulic fracture propagation: A review of recent trends. *Journal of Natural Gas Science and Engineering*, *49*, 66–83. https://doi.org/10.1016/j.jngse.2017.10.012

Lee, H. P., Olson, J. E., Holder, J., Gale, J. F., & Myers, R. D. (2015). The interaction of propagating opening mode fractures with preexisting discontinuities in shale. *Journal of Geophysical Research: Solid Earth*, *120*(1), 169–181. https://doi.org/10.1002/2014jb011358

Lepillier, B., Yoshioka, K., Parisio, F., Bakker, R., & Bruhn, D. (2020). Variational phase-field modeling of hydraulic fracture interaction with natural fractures and application to enhanced geothermal systems. *Journal of Geophysical Research: Solid Earth*, *125*(7), e2020JB019856. https://doi.org/10.1029/2020jb019856

Li, B., & Maurini, C. (2019). Crack kinking in a variational phase-field model of brittle fracture with strongly anisotropic surface energy. *Journal of the Mechanics and Physics of Solids*, *125*, 502–522. https://doi.org/10.1016/j.jmps.2019.01.010

Li, S., Feng, X.-T., Zhang, D., & Tang, H. (2019). Coupled thermo-hydro-mechanical analysis of stimulation and production for fractured geothermal reservoirs. *Applied Energy*, *247*, 40–59. https://doi.org/10.1016/j.apenergy.2019.04.036

Li, S., Zhang, D., & Li, X. (2017). A new approach to the modeling of hydraulic-fracturing treatments in naturally fractured reservoirs. *SPE Journal*, *22*(04), 1064–1081. https://doi.org/10.2118/181828-pa

Li, T., Marigo, J.-J., Guilbaud, D., & Potapov, S. (2016). Gradient damage modeling of brittle fracture in an explicit dynamics context. *International Journal for Numerical Methods in Engineering*, *108*(11), 1381–1405. https://doi.org/10.1002/nme.5262

Li, X., Liang, Y., Luo, Y., & Ai, C. (2020). Predicting hydraulic fracture propagation based on maximum energy release rate theory with consideration of t-stress. *Fuel*, *269*, 117337. https://doi.org/10.1016/j.fuel.2020.117337

Llanos, E. M., Jeffrey, R. G., Hillis, R., & Zhang, X. (2017). Hydraulic fracture propagation through an orthogonal discontinuity: A laboratory, analytical and numerical study. *Rock Mechanics and Rock Engineering*, *50*(8), 2101–2118. https://doi.org/10.1007/s00603-017-1213-3

Marder, M. (2004). Cracks cleave crystals. *EPL*, *66*(3), 364–370. https://doi.org/10.1209/epl/i2003-10254-4

McClure, M. W., & Horne, R. N. (2014). An investigation of stimulation mechanisms in enhanced geothermal systems. *International Journal of Rock Mechanics and Mining Sciences*, *72*, 242–260. https://doi.org/10.1016/j.ijrmms.2014.07.011

Meng, C., & De Pater, C., (2010). Hydraulic fracture propagation in pre-fractured natural rocks. In *44th US rock mechanics symposium and 5th US-Canada rock mechanics symposium*.

Miehe, C., Welschinger, F., & Hofacker, M. (2010). Thermodynamically consistent phase-field models of fracture: Variational principles and multi-field FE implementations. *International Journal for Numerical Methods in Engineering*, *83*, 1273–1311. https://doi.org/10.1002/nme.2861

Naoi, M., Chen, Y., Yamamoto, K., Morishige, Y., Imakita, K., Tsutumi, N., et al. (2020). Tensile-dominant fractures observed in hydraulic fracturing laboratory experiment using eagle ford shale. *Geophysical Journal International*, *222*(2), 769–780. https://doi.org/10.1093/gji/ggaa183

Nishiyama, T., & Kusuda, H. (1994). Identification of pore spaces and microcracks using fluorescent resins. *International Journal of Rock Mechanics and Mining Sciences & Geomechanics Abstracts*, *31*(4), 369–375. https://doi.org/10.1016/0148-9062(94)90904-0

Nocedal, J., & Wright, S. (2006). *Numerical optimization*. Springer Science & Business Media.

Nuismer, R. (1975). An energy release rate criterion for mixed mode fracture. *International Journal of Fracture*, *11*(2), 245–250. https://doi.org/10.1007/bf00038891

Pham, K., Amor, H., Marigo, J.-J., & Maurini, C. (2011). Gradient damage models and their use to approximate brittle fracture. *International Journal of Damage Mechanics*, *20*(4), 618–652. https://doi.org/10.1177/1056789510386852

Renshaw, C., & Pollard, D. (1995). An experimentally verified criterion for propagation across unbounded frictional interfaces in brittle, linear elastic materials. *International Journal of Rock Mechanics and Mining Sciences & Geomechanics Abstracts*, *32*(3), 237–249. https://doi.org/10.1016/0148-9062(94)00037-4

Reynolds, J., Scott, J., Popham, J., & Coffer, H. (1961). Hydraulic fracture-field test to determine areal extent and orientation. *Journal of Petroleum Technology*, *13*(04), 371–376. https://doi.org/10.2118/1571-g

Rice, J. R. (1968). Mathematical analysis in the mechanics of fracture. *Fracture: An Advanced Treatise*, *2*, 191–311.

Riffault, J., Dempsey, D., Karra, S., & Archer, R. (2018). Microseismicity cloud can be substantially larger than the associated stimulated fracture volume: The case of the Paralana Enhanced Geothermal System. *Journal of Geophysical Research: Solid Earth*, *123*(8), 6845–6870. https://doi.org/10.1029/2017jb015299

Schmidt, B., Fraternali, F., & Ortiz, M. (2009). Eigenfracture: An eigendeformation approach to variational fracture. *Multiscale Modeling and Simulation*, *7*(3), 1237–1266. https://doi.org/10.1137/080712568

Schmitt, D. R., & Zoback, M. (1989). Poroelastic effects in the determination of the maximum horizontal principal stress in hydraulic fracturing tests–a proposed breakdown equation employing a modified effective stress relation for tensile failure. *International Journal of Rock Mechanics and Mining Sciences & Geomechanics Abstracts*, *26*(6), 499–506. https://doi.org/10.1016/0148-9062(89)91427-7

Schmitt, D. R., & Haimson, B. (2017). Hydraulic fracturing stress measurements in deep holes. In *Rock mechanics and engineering* (pp. 183–225). CRC Press.

Shimada, T., Ouchi, K., Chihara, Y., & Kitamura, T. (2015). Breakdown of continuum fracture mechanics at the nanoscale. *Scientific Reports*, *5*(1), 1–6. https://doi.org/10.1038/srep08596

Sneddon, I., & Lowengrub, M. (1969). *Crack problems in the classical theory of elasticity*. John Wiley & Sons.

Steinke, C., & Kaliske, M. (2019). A phase-field crack model based on directional stress decomposition. *Computational Mechanics*, *63*(5), 1019–1046. https://doi.org/10.1007/s00466-018-1635-0

Takei, A., Roman, B., Bico, J., Hamm, E., & Melo, F. (2013). Forbidden directions for the fracture of thin anisotropic sheets: An analogy with the wulff plot. *Physical Review Letters*, *110*(14), 144301. https://doi.org/10.1103/physrevlett.110.144301

Timoshenko, S., & Goodier, J. N. (1970). *Theory of elasticity* (3rd ed.). McGraw-Hill.

Wang, K., & Sun, W. C. (2017). A unified variational eigen-erosion framework for interacting brittle fractures and compaction bands in fluid-infiltrating porous media. *Computer Methods in Applied Mechanics and Engineering*, *318*, 1–32. https://doi.org/10.1016/j.cma.2017.01.017

Warpinski, N., & Teufel, L. (1987). Influence of geologic discontinuities on hydraulic fracture propagation. *Journal of Petroleum Technology*, *39*(02), 209–220. https://doi.org/10.2118/13224-pa

Watanabe, N., Egawa, M., Sakaguchi, K., Ishibashi, T., & Tsuchiya, N. (2017). Hydraulic fracturing and permeability enhancement in granite from subcritical/brittle to supercritical/ductile conditions. *Geophysical Research Letters*, *44*(11), 5468–5475. https://doi.org/10.1002/2017gl073898

Wu, J.-Y. (2017). A unified phase-field theory for the mechanics of damage and quasi-brittle failure. *Journal of the Mechanics and Physics of Solids*, *103*, 72–99. https://doi.org/10.1016/j.jmps.2017.03.015

Wu, K., & Olson, J. E. (2016). Numerical investigation of complex hydraulic-fracture development in naturally fractured reservoirs. *SPE Production & Operations*, *31*(04), 300–309. https://doi.org/10.2118/173326-pa

Xu, L. R., Huang, Y. Y., & Rosakis, A. J. (2003). Dynamic crack deflection and penetration at interfaces in homogeneous materials: Experimental studies and model predictions. *Journal of the Mechanics and Physics of Solids*, *51*(3), 461–486. https://doi.org/10.1016/s0022-5096(02)00080-7

Yoshioka, K. (2022). *Data set for hydraulic fracture interactions with discontinuities study*. Zenodo. https://doi.org/10.5281/zenodo.6390977

Yoshioka, K., Katou, M., & Naoi, M. (2022). *Experimental data set for hydraulic fracture interactions with discontinuities study*. Zenodo. https://doi.org/10.5281/zenodo.6811452

Yoshioka, K., Mollaali, M., & Kolditz, O. (2021). Variational phase-field fracture modeling with interfaces. *Computer Methods in Applied Mechanics and Engineering*, *384*, 113951. https://doi.org/10.1016/j.cma.2021.113951

Yushi, Z., Shicheng, Z., Tong, Z., Xiang, Z., & Tiankui, G. (2016). Experimental investigation into hydraulic fracture network propagation in gas shales using CT scanning technology. *Rock Mechanics and Rock Engineering*, *49*(1), 33–45. https://doi.org/10.1007/s00603-015-0720-3

Zeng, X., & Wei, Y. (2017). Crack deflection in brittle media with heterogeneous interfaces and its application in shale fracking. *Journal of the Mechanics and Physics of Solids*, *101*, 235–249. https://doi.org/10.1016/j.jmps.2016.12.012

Zhang, Q., Zhang, X.-P., & Sun, W. (2021). A review of laboratory studies and theoretical analysis for the interaction mode between induced hydraulic fractures and pre-existing fractures. *Journal of Natural Gas Science and Engineering*, *86*, 103719. https://doi.org/10.1016/j.jngse.2020.103719

Zhang, X., Jeffrey, R., Bunger, A., & Thiercelin, M. (2011). Initiation and growth of a hydraulic fracture from a circular wellbore. *International Journal of Rock Mechanics and Mining Sciences*, *48*(6), 984–995. https://doi.org/10.1016/j.ijrmms.2011.06.005

Zhao, Y., Zhang, Y., Wang, C., & Liu, Q. (2022). Hydraulic fracturing characteristics and evaluation of fracturing effectiveness under different anisotropic angles and injection rates: An experimental investigation in absence of confining pressure. *Journal of Natural Gas Science and Engineering*, *97*, 104343. https://doi.org/10.1016/j.jngse.2021.104343

Zhou, J., Chen, M., Jin, Y., & Zhang, G.-Q. (2008). Analysis of fracture propagation behavior and fracture geometry using a tri-axial fracturing system in naturally fractured reservoirs. *International Journal of Rock Mechanics and Mining Sciences*, *45*(7), 1143–1152. https://doi.org/10.1016/j.ijrmms.2008.01.001

Ziaei-Rad, V., Mollaali, M., Nagel, T., Kolditz, O., & Yoshioka, K. (2023). Orthogonal decomposition of anisotropic constitutive models for the phase field approach to fracture. *Journal of the Mechanics and Physics of Solids*, *171*, 105143. https://doi.org/10.1016/j.jmps.2022.105143